Astronomy & Astrophysics manuscript no. jekyll
February 6, 2018

Modelling the spectral evolution of Supernovae.

M. Ergon[1], C. Fransson[1], A. Jerkstrand[2], M. Kromer[3,4], and C. Kozma[1]

[1] The Oskar Klein Centre, Department of Astronomy, AlbaNova, Stockholm University, 106 91 Stockholm, Sweden
[2] Max-Planck-Institut für Astrophysik, Karl-Schwarzschild-Str. 1, D-85748 Garching, Germany
[3] Heidelberger Institut für Theoretische Studien, Schloss-Wolfsbrunnenweg 35, D-69118 Heidelberg, Germany
[4] Institut für Theoretische Astrophysik am Zentrum für Astronomie der Universität Heidelberg, Philosophenweg 12, D-69120 Heidelberg, Germany

To be submitted to Astronomy and Astrophysics.

ABSTRACT

We present JEKYLL, a new code for modelling of SN spectra and lightcurves based on Monte-Carlo (MC) techniques for the radiative transfer. The code assumes spherical symmetry, homologous expansion and steady state for the matter, but is otherwise capable of solving the time-dependent radiative transfer problem in non-local-thermodynamic-equilibrium (NLTE). **The method used was introduced in a series of papers by Lucy**, and we have extended it to include non-thermal excitation and ionization as well as charge-transfer and two-photon processes. Macroscopic mixing of the material, known to occur in the SN explosion, **is taken into account in a statistical sense**. To save computational power we use a **diffusion solver** in the inner region, where the radiation field is thermalized. Except for a description of JEKYLL, we provide comparisons with the ARTIS, **SUMO and CMFGEN codes, which show good agreement in the calculated spectra as well as the state of the gas**. We also provide an application to Type IIb SNe, by calculating the early (before 150 days) evolution for a model previously found to give a good match to SN 2011dh in the nebular phase. A thorough comparison to observations of SN 2011dh is made, and we find that both spectra and lightcurves are reasonably well reproduced, although there are also clear differences. In a broader context the model reproduces many features of Type IIb SNe that have previously been noted in observational studies. Comparing to results where NLTE was partly switched off as well as to previous results with the LTE-based HYDE code, we find strong effects of NLTE even on the bolometric lightcurve. This highlights the need for full NLTE calculations when simulating the spectra and lightcurves of SNe. Comparing to results where macroscopic mixing was switched off, we find strong effects on the spectra after ∼50 days, and the model using microscopic mixing has much stronger calcium lines than observed. This shows that both NLTE and macroscopic mixing are essential ingredients in simulations that extend beyond the diffusion phase.

Key words. supernovae: general

1. Introduction

Modelling the spectral evolution and lightcurves of supernovae (SNe) is crucial for our understanding of these phenomena, and much effort has been put into this during the last 50 years. To achieve realistic results local thermodynamic equilibrium (LTE) can generally not be assumed, and the full frequency-dependent, non-LTE (NLTE) problem has to be solved. Several paths exist and here we follow the one outlined in a series of papers by Lucy (2002, 2003, 2005, hereafter L02, L03, L05). Using this method, the radiative transfer is solved by a Monte-Carlo (MC) calculation, which is alternated with a NLTE solution for the matter until convergence is achieved (Λ-iteration). Basic tests were performed in the original papers, and a simplified version of the method, assuming LTE for the population of excited states, has been implemented in the code ARTIS (Kromer & Sim 2009, hereafter K09). Several other codes, as e.g. TARDIS (Kerzendorf & Sim 2014) and SEDONA (Kasen et al. 2006) are also based on the method (or parts of it), but are all simplified in one way or another. Here we present JEKYLL, a C++ based code which implements the full NLTE-version of the method, extended to include also non-thermal excitation and ionization as well as charge-transfer and two-photon processes. These extensions are particularly important for modelling in the nebular phase, and for the calculation of the non-thermal rates we use the method developed by Kozma & Fransson (1992, hereafter KF92). Contrary to ARTIS, the initial version of JEKYLL is restricted to a spherical symmetric geometry, although the MC radiative transfer is performed in 3-D. In the paper, we present comparisons with ARTIS as well as the steady-state **NLTE** code SUMO **(Jerkstrand et al. 2011, 2012, hereafter J11,J12)** aimed for the nebular **(optically thin)** phase, **and the general purpose NLTE code CMFGEN (Hillier & Miller 1998, hereafter H98)**. **CMFGEN uses traditional techniques to solve the NLTE problem, but is otherwise similar to JEKYLL. The three comparisons with ARTIS, SUMO and CMFGEN provide a critical test of the functionality of JEKYLL.**

Type IIb SNe are thought to originate from stars that have lost most, but not all of their hydrogen envelope. Except for the prototypical Type IIb SN 1993J, the most well-observed Type IIb SN is 2011dh, for which we presented observations and modelling of the lightcurves in Ergon et al. (2014, 2015, hereafter E14, E15), as well as modelling of nebular spectra in Jerkstrand et al. (2015, hereafter J15). The modelling suggested a mass of $\sim$12 $M_\odot$ for the progenitor, a conclusion supported by observations of the star in pre-explosion images (Maund et al. 2011). As stellar winds for stars of this mass seem too low to expel the hydrogen envelope this suggests a binary origin, where the hydrogen envelope was lost through interaction with a companion star. A similar conclusion, based on modelling of the SN, pre-explosion observations of the progenitor star, as well as a likely

post-explosion detection of the companion star, applies to SN 1993J. It is therefore of great interest to further explore the preferred 12 $M_\odot$ model presented in J15, evolved through the nebular phase using SUMO, and compared to the observed spectra and lightcurves of SN 2011dh in J15 and E15, respectively. This model was also evolved through the early phase using the hydrodynamical, LTE-based code HYDE in E15, allowing a comparison of the bolometric lightcurve with observations. Using JEKYLL we are able to calculate the early spectral evolution, as well as the broadband and bolometric lightcurves in much greater realism, and compare to observations as well as to the results obtained with HYDE.

The paper is organized as follows. In Sect. 2 we discuss the underlying physical problem, and in Sect. 3 we describe the method used to solve this problem and the design of the code. In Sect. 4 we provide comparisons of JEKYLL to the ARTIS and SUMO codes. In Sect. 5 we apply the code to Type IIb SNe, calculate the early spectral evolution for the preferred J15 model, and discuss and compare the results to observations of SN 2011dh. Finally, in Sect. 6 we conclude and summarize the paper.

2. Physics

The general physical problem adressed is the time-evolution of the radiation field and the state of the matter given the dynamical constraint of homologous expansion, and might be referred to as a radiation-thermodynamical problem. If the radiation field and the matter are in local thermodynamic equilibrium (LTE) this is simplified to a one-parameter (i.e the temperature) problem, and may be easily solved. Otherwise, we are in the non-LTE (NLTE) regime, and the number of parameters as well as the complexity of the problem increase drastically.

As is often done, we solve for the radiation field and state of the matter separately, and the problem is split into a radiative transfer and a thermodynamical part. The coupling, provided by radiation-matter interactions, is enforced through Λ-iterations, where the state of the matter and the radiation field are alternately and iteratively determined from each other. The Λ-iteration concept is at the heart of the method, and in Sect. 2.1 we provide some background and discuss the somewhat different meaning it has in traditional and MC based methods.

The state of the matter can be separated into a dynamical and thermodynamical part, where the former is trivially given by $\rho = \rho_0 \, (t/t_0)^3$ and $v = r/t$ through the constraint of homologous expansion. The thermodynamical part is given by the temperature, and the populations of ionized and excited states, which are solved for using the thermal energy equation and the NLTE rate equations, respectively. To simplify we assume steady state, which is motivated if the thermodynamical time-scale is much smaller than the dynamical time-scale.

The radiation field is given by the specific intensity, which is solved for using the MC method outlined by L02, L03 and L05, and discussed in Sect. 3.3. In a traditional code like CMFGEN, the specific intensity is solved for using the radiative transfer equation, whereas in a MC based code like JEKYLL, the radiative transfer is treated explicitly by propagating radiation packets which interact with the matter through absorption, emission and scattering. The different radiation-matter interactions supported are discussed in Sect. 2.4.

In addition, radioactive decays emit high-energy photons or leptons, which give rise to a non-thermal electron distribution. Through collisions, these electrons contribute to the heating of the electron gas and the excitation and ionization of the ions. The problem may be broken up into two parts; deposition of the radioactive decay energy, and the partitioning of this energy into non-thermal heating, ionization and excitation.

2.1. Λ-iterations and convergence

In terms of the Λ-operator the radiative transfer equation may be written as $I = \Lambda[S]$, where I is the intensity and S the source-function. If the source function depends on the intensity, as in the case of scattering, solving the problem requires inverting the Λ-operator. This is typically a costly operation, and we may instead try an iterative procedure called Λ-iteration (see e.g. Hubeny & Mihalas 2014). In its original form an improved estimate of the intensity is then determined using the previous estimate of the source-function, i.e. $I_{i+1} = \Lambda[S_i]$. However, this method may converge extremely slowly if the source function is dominated by scattering, as the non-local coupling introduced only propagates one mean-free path per iteration. This may be solved by splitting the Λ-operator in two parts, one acting on the current iteration and one acting on the previous iteration, i.e. $I_{i+1} = \Lambda^*[S_{i+1}] + (\Lambda - \Lambda^*)[S_i]$. With an appropriate choice of Λ^*, e.g the local part of Λ, which is trivial to invert and still close to Λ, convergence could be accelerated, and the procedure is therefore known as accelerated Λ-iteration (see e.g. Scharmer 1984, Werner & Husfeld 1985 and Olson et al. 1986).

It is important to realize that the explicit dependence of the scattering emissivity on the intensity does not cause slow convergence in the MC case. The reason for this is that the MC scattering emissivity depends directly on the current iteration of the MC radiation field. **Actually, a MC Λ-iteration is similar** to an accelerated Λ-iteration in the sense that the current iteration depends partly on itself. Enforcing the constraints of thermal and statistical equilibrium on the MC calculation, introduces a direct (but approximate) dependence of all MC emissivities on the current iteration of the MC radiation field, which further **accelerates the convergence**. This idea is central for the method outlined by L02-L05, and as demonstrated in L03, Λ-iterations based on this **method** have excellent convergence properties.

2.2. Statistical equilibrium

To determine the populations of ionized and excited states, the NLTE rate equations need to be solved. Assuming steady state, these equations simplify to the equations of statistical equilibrium, where the rates of transitions in and out of each state are in equilibrium. The statistical equilibrium equation for level i of ion I may be written

$$\sum_{J=I\pm1} r^{\mathrm{BF}}_{J,j\rightarrow I,i}\, n_{J,j} + \sum_{j\neq i} r^{\mathrm{BB}}_{I,j\rightarrow i}\, n_{I,j} = \left(\sum_{J=I\pm1} r^{\mathrm{BF}}_{I,i\rightarrow J,j} + \sum_{j\neq i} r^{\mathrm{BB}}_{I,i\rightarrow j} \right) n_{I,i} \tag{1}$$

where r is **the rate** (per particle) for bound-free (superscript BF) and bound-bound (superscript BB) transitions, and n is the number density. **Note that the equation system is non-linear as (some) transition rates (per particle) depends on the number densitities.** Transitions may be caused by absorption/emission of photons (Sect. 2.4), or by collisions involving ions and thermal (Sect. 2.5) or non-thermal (Sect 2.6.1) electrons.

2.3. Thermal equilibrium

To determine the thermal state of the gas the thermal energy equation needs to be solved. Assuming steady state, this equation simplifies to the equation of thermal equilibrium, where the heating and cooling of the gas are in equilibrium. The thermal equilibrium equation may be written

$$\sum_{J=I\pm1} g^{\mathrm{BF}}_{I,i\rightarrow J,j}(T)\, n_{I,i} + \sum_{i\neq j} g^{\mathrm{BB}}_{I,i\rightarrow j}(T)\, n_{I,i} + \sum g^{\mathrm{FF}}_{I}(T)\, n_{I,i} = H^{\mathrm{NT}} \quad (2)$$

where g is the net heating rate (per particle) for bound-free (superscript BF), bound-bound (superscript BB) and free-free (superscript FF) transitions, and H^{NT} is the heating rate by non-thermal collisions. Heating/cooling may arise through absorption/emission of photons (Sect. 2.4), or through collisions involving ions and thermal (Sect. 2.5) or non-thermal (Sect 2.6.1) electrons.

2.4. Radiation-matter interactions

In radiation-matter interactions, the radiation field and the matter (electrons and ions) exchange energy through absorption and emission of photons. Except for electron scattering, which is assumed to be coherent and isotropic in the co-moving frame (of the ejecta), and given by the Thomson cross-section, JEKYLL supports the following interactions.

Bound-bound Through detailed balance, the excitation and de-excitation rates are related and determined by a single quantity, e.g. the spontaneous emission coefficient. We assume that the Sobolev approximation **(Sobolev 1957)** applies, which is appropriate when expansion broadening dominates. Expressions for the Sobolev optical depth as well as the transition rates are given in L02. In addition, we also support de-excitation through two-photon emission for bound-bound transitions otherwise radiatively forbidden.

Bound-free Through detailed balance, the ionization and recombination rates are related and determined by a single quantity, e.g. the photo-ionization cross-section. In bound-free transitions, the energy absorbed/emitted goes partly into ionization/recombination of the ion, and partly into heating/cooling of the electron gas. Expressions for the opacity, emissivity, transition rates and heating/cooling rates are given in L03.

Free-free Refers to Bremsstrahlung, and assuming thermal matter, the opacity and emissivity are related through Kirchoffs law. In free-free interactions, the energy of the photons absorbed/emitted goes solely into heating/cooling of the electron gas. Expressions for the opacity, emissivity, and heating/cooling rates are given in L03.

2.5. Matter-matter interactions

In matter-matter interactions, electrons and ions exchange energy through collisions. The collisions heat/cool the electron gas and result in bound-bound or bound-free transitions of the ions. Except for non-thermal collisions, which are discussed in Sect. 2.6.2, JEKYLL supports the following interactions.

Bound-bound and bound-free Through detailed balance, the collisional excitation and de-excitation rates are related and determined by a single quantity, e.g. the collisional strength. The same is true for the collisional ionization and recombination rates, and expressions for the transition rates and heating/cooling rates are given in L03.

Charge-transfer In collisions involving two ions, electrons may be transferred from one ion to another. This process is called charge-transfer and may be viewed as a recombination followed by a ionization. The charge transfer rates may be expressed in terms of a charge-transfer coefficient (α) that depends only on the temperature as

$$\begin{aligned} R_{\bar{I},\bar{J}\rightarrow\bar{U},\bar{L}} &= \alpha_{\bar{I},\bar{J}\rightarrow\bar{U},\bar{L}}(T)\, n_{\bar{I}}\, n_{\bar{J}} \\ R_{\bar{U},\bar{L}\rightarrow\bar{I},\bar{J}} &= \frac{\alpha_{\bar{I},\bar{J}\rightarrow\bar{U},\bar{L}}(T)}{\phi_{\bar{I},\bar{J},\bar{U},\bar{L}}(T)}\, n_{\bar{U}}\, n_{\bar{L}} \end{aligned} \quad (3)$$

where $\phi_{\bar{I},\bar{J},\bar{U},\bar{L}}(T) = (n^*_{\bar{I}}\, n^*_{\bar{J}})/(n^*_{\bar{U}}\, n^*_{\bar{L}})$, the asterisk indicates the LTE value and $\bar{I} = (I, i)$ is an index vector specifying **level** i **of ion** I. The energy difference between the initial and final state of the process gives rise to heating or cooling of the electron gas with a rate given by $R_{\bar{I},\bar{J}\rightarrow\bar{U},\bar{L}}\ \left|\chi_{\bar{I},\bar{U}} - \chi_{\bar{L},\bar{J}}\right|$, where χ is the ionization energy.

2.6. Radioactive decays

2.6.1. Energy deposition

The energy released in the radioactive decays is carried by high-energy photons and leptons which deposit their energy in the ejecta mainly through Compton scattering on free and bound electrons. Although a detailed calculation is preferred, we use effective grey opacities determined through such calculations. We **support the** decay chains ^{56}Ni $\rightarrow$ ^{56}Co $\rightarrow$ ^{56}Fe, ^{57}Ni $\rightarrow$ ^{57}Co $\rightarrow$ ^{57}Fe and ^{44}Ti $\rightarrow$ ^{44}Sc $\rightarrow$ ^{44}Ca, which are the most important for core-collapse SNe. For these decays we adopt the life-times and **energies** from Kozma & Fransson (1998) and the effective grey γ-ray opacities from J11, and assume that the positrons emitted are locally absorbed.

2.6.2. Energy partition

Through a cascade of collisions the deposited energy gives rise to a high-energy tail on the otherwise Maxwellian electron distribution. The shape of the non-thermal electron distribution and the fractions of the energy going into heating, excitation and ionization through non-thermal collisions can be calculated by solving the Spencer-Fano equation (Boltzman equation for electrons). This problem was solved by KF92 and for a further discussion we refer to this paper.

3. Method and design

Given the physical problem, we now describe the methods used to solve it, and provide an outline of how the code is designed. Except for the non-thermal solver, the code is written in C++, and the description therefore tends to reflect the object oriented structure of the code. The code is parallelized on a hybrid process (MPI) and thread **(openMP)** level.

The SN ejecta **are** represented by a spatial grid of cells holding the local state of the matter and the radiation field. Although

mostly geometry independent, the current version only supports spherically symmetric cells. To determine the state of the matter, JEKYLL provides several solvers with different levels of approximation (e.g. LTE and NLTE), and to determine the radiation field it provides a MC solver based on the method by L02-L05. As discussed, through Λ-iterations the matter and the radiation field are alternately determined from each other, a procedure which in JEKYLL is terminated after a fixed but configurable number of iterations. JEKYLL also provides a diffusion solver, intended for use at high optical depths where the matter and radiation field may be assumed to be in LTE. JEKYLL may be configured to run in steady-state or time-dependent mode, although the latter only applies to the radiative transfer. Steady-state **for the radiation field** breaks down if the diffusion time is large, and is therefore best suited for modelling in the nebular (optically thin) phase, or of the SN atmosphere in the photospheric (optically thick) phase.

3.1. Grid

The grid represents the SN ejecta and is spatially divided into a number of cells, which in the current version of the code are spherically symmetric. If macroscopic mixing is used, the cells may be further divided into compositional zones, geometrically realized as virtual cells. The grid provides functions to load the ejecta model, to load and save the state, as well as to export a broad range of derived quantities (e.g. opacities).

3.1.1. Cells

The cells hold the local state of the matter and the radiation field, and provide functions for the solvers to calculate derived quantities like opacities/emissivities and transition rates based on the local state and the atomic data. The local state of the matter is represented by the density, the temperature, and the number fractions of ionized and excited states. The local state of the radiation field is represented by the specific intensity, which is updated by the MC radiative transfer solver based on packet statistics following the method outlined by L03. In addition, JEKYLL supports simplified radiation field models based on pure or diluted blackbody radiation given by $B_\nu(T_J)$ and $WB_\nu(T_R)$, respectively (see K09 for details). **JEKYLL also allows the radiation-field to be approximated by the bound-free source-function as $I = S^{\mathrm{BF}}(\mathbf{n}, T)$, which depends only on the local state of the matter. This option** is intended for use in ground-state continua of abundant species, which typically have high optical depths and are dominating the source-function.

3.1.2. Virtual cells

JEKYLL implements the concept of virtual cells, introduced by J11 to account for macroscopic mixing on a grid otherwise spherically symmetric. Each cell may be divided into zones occupying some fraction (filling factor) of the cell volume, and otherwise geometrically unspecified. These zones may have different densities and compositions, and the state is solved for separately by the matter-state solver. With respect to the MC-solver the zones are represented by virtual cells differing only in a geometrical and statistical sense. The virtual cells are spherical, have a size corresponding to some number of clumps, and their location is randomly drawn during the MC radiative transfer based on their size and the zone filling factor.

3.2. Atomic data

Once converted to the JEKYLL format, any set of atomic data may be loaded from file. The data is organized in a hierarchical structure of atoms, their isotopes and ions, and the bound states of the ions. Each ion holds a list of bound-bound transitions, and each atom holds a list of bound-free transitions. The atomic data also contains an (optional) list of charge-transfer reactions, which are mapped on two bound-free transitions, one recombination and one ionization. The specific atomic data used for the comparisons in Sects. 4.1 and 4.2 and for the application to Type IIb SNe in Sect. 5 are discussed in Appendix A. The latter, which is the default choice, is inherrited from SUMO (see J11 and J12), and extended as described in Appendix A.4.

3.3. MC radiative transfer solver

The MC radiative transfer solver determines the radiation field, and is based on the method outlined in L02-L05. The radiation field is discretized as packets (Sect. 3.3.1), which are propagated on the grid (Sect. 3.3.2) and interact with the matter (Sect. 3.3.3). In the calculation, the constraints of statistical and thermal equilibrium are enforced, which accelerates the convergence of the Λ-iterations (see Sect.2.1). The method has been extended to include non-thermal ionizations and excitations as well as charge-transfer and two-photon processes. In addition, we introduce an alternative, more efficient way to draw the emission frequency (Sect. 3.3.4), and a method to control the sampling of the radiation field (Sect. 3.3.5). Although we explain the basics, we refer to L02-L05 for the details of the original method.

3.3.1. Packets

The radiation field is discretized as packets, defined by their energy, frequency, position and direction. Following L03 and K09, we classify these as r-, i-, k- and γ-packets. The packets are indivisible and indestructible (but see Sect. 3.3.5 for a modified requirement), which enforce the constraint of thermal equilibrium on the MC calculation. Freely propagating photons are represented by r-packets, and upon absorption they are converted into i- and k-packets, representing ionization/excitation and thermal energy, respectively. The γ-packets are similar to the r-packets, but represent the γ-rays (or leptons) emitted in the radioactive decays, which are treated separately. Eventually, the i- and k-packets are converted into r-packets and re-emitted.

New r-packets are injected into the MC-calculation by sampling of the luminosity at the inner border (if any), and new γ-packets by sampling of the γ-ray emissivity. In addition, r-packets may be initially sampled from the intensity in each cell, as well as from new cells taken over from the diffusion solver when the inner border is moved inwards.

3.3.2. Propagation

When the r- and γ-packets are propagated they undergo physical (radiation-matter interactions) and geometrical (border crossings) events. Whereas propagation is carried out in the rest frame, the physical events take place in the co-moving frame, and the packets are transformed back and forth to $O(v/c)$. After each event, a random optical depth for the next physical event is drawn as $\tau = -\ln z$, and the packet is propagated until the accumulated optical depth exceeds this value or a geometrical event occurs. Note that line-absorption may only occur at the resonance distances, and the (Sobolev) line-opacity may be re-

garded as a delta-function. In the case of a physical event, the packet is processed as described in Sect. 3.3.3, and in either case propagation continues as described above. Note, that in the case of γ-packets we use effective grey opacities (Sect 2.6.2), which differs from the more detailed procedure by L05. The r- and γ-packets leave the MC calculation by escaping through the outer border, where the r-packets are binned and summed to build the observed spectrum.

If the packet enters a cell divided into compositional zones (Sect. 3.1.2), a randomly oriented virtual cell is drawn based on the filling factor of the corresponding zone **(see J11 for details)**. As long as the packet remains in the cell, the distance to the next geometrical event is given by the size and the orientation of the virtual cell, and at each (virtual) border crossing the procedure is repeated.

3.3.3. Interactions

Once the packet has been absorbed, the type of interaction is drawn in proportion to the opacities. In the case of electron scattering, the frequency does not change. Otherwise, an emission frequency is drawn using the method described by L02 and L03, which enforces the constraints of statistical and thermal equilibrium on the MC calculation. Below we provide a summary of the method and describe the extensions made for non-thermal, charge-transfer and two-photon processes. Before re-emission of the packet a new direction is drawn from an isotropic distribution.

Original method To enforce the aforementioned constraints on the MC calculation, L02 and L03 introduce the concepts of macro-atoms and the thermal pool, which are the MC analogues of the statistical and thermal equilibrium equations. The macro-atoms are state-machines mirroring the energy structure of the atomic species, and are activated by upward transitions (e.g. excitations) and de-activated by downward transitions (e.g. de-excitations). In de-activations through radiative transitions, i-packets are converted to r-packets and re-emitted, whereas in de-activations through collisional transitions, i-packets are converted to k-packets and transferred to the thermal pool. The k-packets enter the thermal pool through radiative and collisional heating and leave through radiative and collisional cooling, in which case they are converted into r- or i-packets in proportion to the cooling rates. Together, the macro-atoms and the thermal pool constitute a single state-machine activated by an absorption of a r- or γ-packet, and de-activated by the emission of a r-packet. The absorbed r- and γ-packets are converted into i- or k-packets in proportion to the energy going into ionization/excitation and heating. The frequency of the emitted r-packet is drawn from the (normalized) emissivity of the de-activating process.

Although the method is conceptually simple, it is a bit involved in the details, not the least with respect to the macro-atoms. These are activated either by radiative or collisional upward transitions (e.g. excitations), drawn in proportion to their opacities and cooling rates, respectively. If a macro-atom is activated at level i, each physical transition with number rate $R_{i,j}$ corresponds to an internal state-machine transition with probability $p_{i,j} \propto R_{i,j}E_l$ (L02: Eq. 9), where E_l is the energy of level $l = min(i, j)$. In addition, each physical downward transition (e.g. de-excitation) may de-activate the macro-atom with probability $p_{i,l} \propto R_{i,l}(E_i - E_l)$ (L02: Eq. 7). If an internal transition is drawn the state-machine proceeds to level j and the procedure is repeated.

Non-thermal processes Upon absorption, γ-packets are converted into i- or k-packets in proportion to the energy going into ionization/excitation and heating. This differs from the original method where only the heating channel was allowed. In the case of an i-packet, a macro-atom state-machine is activated by a non-thermal transition drawn in proportion to its energy rate. The macro-atom state-machines are modified by adding the probabilities for non-thermal transitions calculated from their number rates as explained above. Non-thermal transitions are upward, and therefore correspond to internal transitions.

Charge-transfer processes As mentioned, charge-transfer is a collisional process that may be viewed as a recombination followed by an ionization, where the (small) energy difference results in either heating or cooling. The macro-atom state-machines are therefore modified by adding the probabilities for the corresponding ionizations and recombinations calculated from their number rates as explained above. Charge-transfer ionizations correspond to internal transitions, whereas charge-transfer recombinations correspond to internal and de-activating transitions.

De-activation of a macro-atom state-machine through a charge-transfer recombination results in either activation of another macro-atom state-machine through the corresponding ionization or in the conversion of the i-packet into a k-packet. The latter corresponds to the conversion of ionization energy into thermal energy, may only happen if the reaction is exo-thermic, and is drawn in proportion to the energy going into heating. Correspondingly, if the reaction is endo-thermic, k-packets may be converted into i-packets, and a macro-atom state-machine activated by the corresponding ionization. This corresponds to the conversion of thermal energy into ionization energy, and is drawn in proportion to the cooling rate as described above.

Two-photon processes The macro-atom state-machines are modified by adding the probabilities for two-photon transitions calculated from their number rates as explained above. Two-photon transitions are downward, and might therefore be either internal or de-activating, and in the latter case the emission frequency is drawn from the (normalized) two-photon emissivity.

3.3.4. Markov-chain solution to the state-machine

A problem with the original method is that the number of transitions in the state-machine may become very large. This is particularly true when the collisional rates are high, causing the state-machine to bounce back and forth between macro-atoms and the thermal pool. To avoid this we use Markov-chain theory to calculate the probabilities to escape the state-machine by a de-activating transition. This approach can be applied individual to macro-atoms, or to the complete state-machine. According to Markov-chain theory, the average time spent in state i, given that the machine is invoked in state j, **is** specified by the matrix $S_{i,j}$. **This matrix** can be calculated from the matrix $P_{i,j}$, containing the probabilities for internal transitions from state i to state j, through the relation $S^{-1} = P - I$, **where I is the identity matrix**. Knowing S, we may proceed to the state from which the machine will de-activate by a single draw, and once there, we may draw the de-activating transition from their (normalized) probabilities. This is implemented as two look-up tables for each bound state, one containing (a row of) S, and one containing the (normalized) de-activating transition probabilities.

Applied to the complete state-machine, the matrix S has size $N \times N$, where N is the total number of energy levels for all atoms plus one (the thermal pool), and the computational time to invert the matrix is a potential problem. This may be circumvented by splitting the state-machine into top-level and atom-level parts, and calculate the corresponding S-matrices separately. The procedure is similar to what is described above, but the computational time to invert the top-level and atom-level S-matrices is much less than for the complete S-matrix.

3.3.5. Controlling the sampling of the radiation field

Another problem with the original method is that there is no (or limited) control of the number of packets as a function of frequency, space and time. This may result in too few packets, leading to noise in the radiation field estimators, or too many, leading to unnecessary computational effort. To solve this we introduce a method for continuous re-sampling of the packets by **allowing** their energy vary as a function frequency, space and time. This breaks the indivisibility and destructibility requirements introduced by L02, but conservation of packet energy, **which is the essential property**, is still maintained in an average sense.

A set of sampling regions (bounded in frequency, space and time) is defined, and each of these is assigned a packet energy. When packets cross the borders between sampling regions, their energy is adjusted to that of the destination region. To maintain the rate of energy flowing across the borders, the rate of packets flowing across the borders has to be adjusted with the ratio of the packet energies in the source and destination regions (F). **When borders are crossed due to motion, this is achieved by splitting the packets into F child packets (if F>1) or terminating them with probability 1-F (if F<1). When (frequency) borders are crossed due to interactions with the matter**, this is achieved by adjusting the emission rates with F and **by introducing** a fictitious opacity (κ_F) corresponding to the total adjusted emission rate (which may be higher or lower than the original one). Although the basic idea is **straightforward**, the actual implementation is complicated by the way the emission frequency is drawn (Sect. 3.3.3).

Replacing κ with $max(\kappa, \kappa_F)$, packets are selected for either absorption, emission or both. The packet is absorbed with probability $max(\kappa/\kappa_F, 1)$ and emitted with probability $max(\kappa_F/\kappa, 1)$. If the packet is absorbed but not emitted it is terminated, and if the packet is emitted but not absorbed a child packet is created. Otherwise the transition is handled as described above (which also recovers the normal behaviour if $\kappa = \kappa_F$). As is possible to show, this gives the correct (average) energy flows in and out of each sampling region. **When using the method, the number of packets is controlled by continuosly adjusting the packet energy in each sampling region. In JEKYLL, this is done once each Λ-iteration based on packet statistics from the previous Λ-iteration**.

3.4. Matter state solvers

To determine the state of the matter, JEKYLL provides the NLTE solver, as well as the more approximate LTE and **Mazzali & Lucy (1993, hereafter ML93)** solvers. It also provides an option to mix these solvers, e.g. by using the NLTE solver for the ionization and the LTE solver for the excitation, in a manner similar to what is done in ARTIS. In addition, JEKYLL provides a solver to determine the non-thermal electron distribution, used by the NLTE solver.

3.4.1. LTE solver

The LTE solver determines the state of the matter assuming that LTE applies. The populations of ionized **and** excited states are calculated using the Saha ionization and Boltzman excitation equations, respectively. The temperature used may be **that associated with the pure or diluted blackbody radiation field models (T_J or T_R; see Sect. 3.1.1 and K09)**, or the matter temperature determined by some other method **(e.g. thermal equilibrium)**.

3.4.2. ML93 solver

The ML93 solver determines the state of the matter assuming that the radiative rates **dominate**, and is based on the approximations for the populations of ionized and excited states derived by Mazzali & Lucy (1993) and Abbott & Lucy (1985). Following Mazzali & Lucy (1993), the temperature is assumed to be controlled by the radiation field and set to $0.9T_R$, where T_R is the temperature **associated with the diluted blackbody radiation field model (see Sect. 3.1.1 and K09)**.

3.4.3. NLTE solver

The NLTE solver determines the state of the matter by solving the statistical and thermal equilibrium equations for the level populations and the temperature, respectively. The solution is determined in two steps. First, thermal equilibrium is scanned for in a configurable temperature interval (based on the solution from a previous Λ-iteration), solving for statistical equilibrium at each step. Based on this estimate, thermal and statistical equilibrium are simultaneously iterated for until convergence is achieved, using a procedure similar to what is described by L03.

Statistical equilibrium The non-linear statistical equilibrium equation system (Eq. 1) is solved by iteration on the level populations. In each step the system is linearised in terms of changes in the level populations, and the rates and their derivatives are calculated using the previous estimate of these. The linearised system is then solved for the level populations using lower-upper (LU) decomposition and back-substitution. If all number derivatives (explicit and implicit) are included this is equivalent to a Newton-Raphson solver, but we leave this as a configurable choice, and in the simplest configuration only the explicit derivatives (i.e. rates per particle) are included.

The equation system may be solved separately for the states of each atom, ignoring any coupling terms, or for all states at once. As the total number of states may be too large for a coupled solution, we provide the possibility to alternate a decoupled solution with a fully coupled solution for the ionization balance. Typically a decoupled solution works well, but charge-transfer reactions and the source-function radiation field model (see Sect. 3.1.1) may introduce strong coupling terms. Transition rates (Sects. 2.4 and 2.5) for bound-bound and bound-free radiative and collisional processes, as well as for non-thermal, charge-transfer and two-photon processes are all supported, but which ones to include is a configurable choice.

Thermal equilibrium The thermal equilibrium equation (Eq. 2) is solved either using the **bisection** method (initial estimate) or Newton-Raphson's method (refined estimate), in which case an explicit temperature derivative is used. Heating and cooling rates (Sects. 2.4 and 2.5) for bound-bound and bound-free ra-

diative and collisional processes, free-free processes, as well as non-thermal and charge-transfer processes are all supported, but which ones to include is a configurable choice. In addition, an expansion cooling term PdV/dt may also be included, as is motivated in a time-dependent run.

3.4.4. Non-thermal solver

The non-thermal solver determines the non-thermal electron distribution resulting from the radioactive decays, and the fraction of the deposited energy going into heating, excitation and ionization. This is done by solving the Spencer-Fano equation (i.e. the Boltzman equation for electrons) as described in KF92.

3.5. Diffusion solver

The diffusion solver determines the temperature in each cell by solving the thermal energy equation assuming spherical symmetry, homologous expansion, LTE and the diffusion approximation for the radiative flux. This results in a non-linear equation system for the temperature in each cell, which is solved by a Newton-Raphson like technique similar to the one used by Falk & Arnett (1977). Two specific topics require some further discussion though; the Rosseland mean opacity used in the diffusion approximation, and the outer boundary where the diffusion solver is supposed to be coupled to the MC radiative transfer solver.

3.5.1. Opacity

The Rosseland mean opacity used in the diffusion approximation is calculated from the LTE state of the matter and the atomic data. This may sound straightforward, but the bound-bound opacity, and in particular the virtual cell mode (see Sect 3.1.2) complicates things. In the latter case, if the clumps are all optically thin, the opacity may be calculated as a zone average, but otherwise a geometrical aspect enters the problem. Therefore we calculate the Rosseland mean opacity using **a** Monte-Carlo method. In each cell a large number of packets are sampled based on the blackbody flux distribution and the zone filling factors. These packets are then followed until they are absorbed, and their path-length averaged to get the Rosseland mean free path. This gives the Rosseland mean opacity, including the bound-bound contribution as well as the geometrical effects arising in a clumpy **material.**

3.5.2. Outer boundary

If the diffusion solver is coupled to the MC radiative transfer solver at the outer boundary **(which is the main purpose of it)**, appropriate boundary conditions must be specified for both solvers. As outer boundary condition for the diffusion solver we use the temperature in the innermost cell handled by the MC radiative transfer solver. **As** inner boundary condition for the MC radiative transfer solver we use the luminosity at this boundary determined with the difussion solver. To implement the latter condition we use an approximate method. **During a timestep Δt, packets with total energy** $L\Delta t$ are injected at the inner boundary, whereas packets propagating inwards are simply reflected at this boundary. The frequency of the injected packets are sampled from a blackbody distribution at the temperature of the innermost cell.

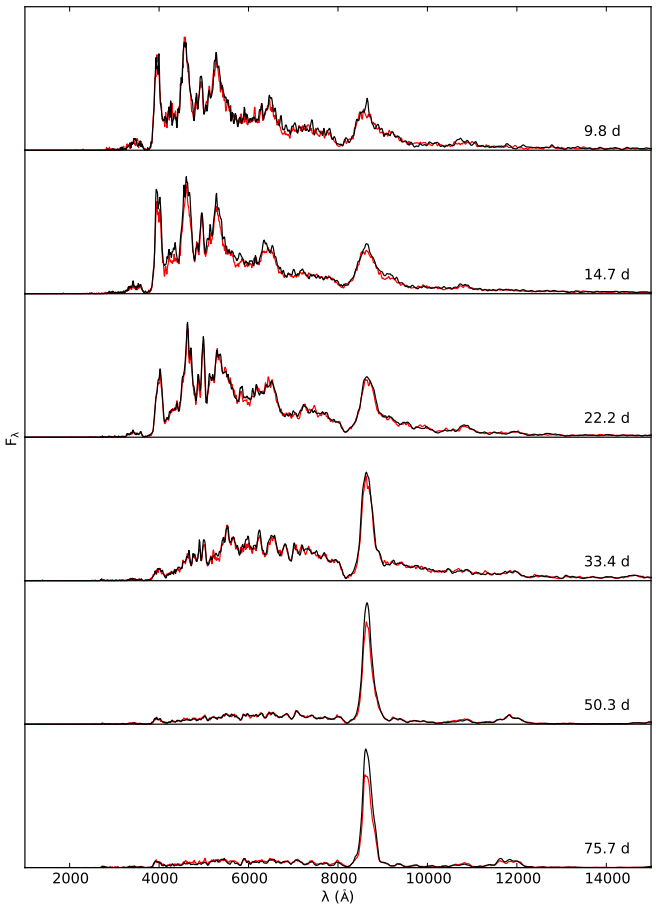

Fig. 1. Comparison of spectral evolution for model 12C as calculated with JEKYLL (black) and ARTIS (red).

4. Comparisons

In this section we compare JEKYLL to **ARTIS (K09), SUMO (J11 and J12), and CMFGEN (H98), three** codes which have similar, but not identical capabilities. ARTIS provides a good test of the time-dependent MC radiative transfer, which is very similar, but only supports partial NLTE. SUMO on the other hand, provides a good test of the full NLTE problem, but requires steady-state, so no test of the time-dependent MC radiative transfer is possible. **On the contrary, CMFGEN, which is similar to JEKYLL in physical assumptions but different in technique, do provide a test of the full time-dependent NLTE problem. An in-depth comparison to this code is highly motivated but outside the scope of the paper. Here we present a first comparison for a somewhat simplified test case, which still provide a good test of the full time-dependent NLTE problem.**

The comparisons to ARTIS, SUMO and CMFGEN are complementary, and taken together they provide a **thorough** test of the JEKYLL code.

4.1. Comparison with ARTIS

ARTIS is a spectral synthesis code aimed for the photospheric phase presented in K09. Both ARTIS and JEKYLL are based on the method outlined in L02-L05, but ARTIS only supports a sim-

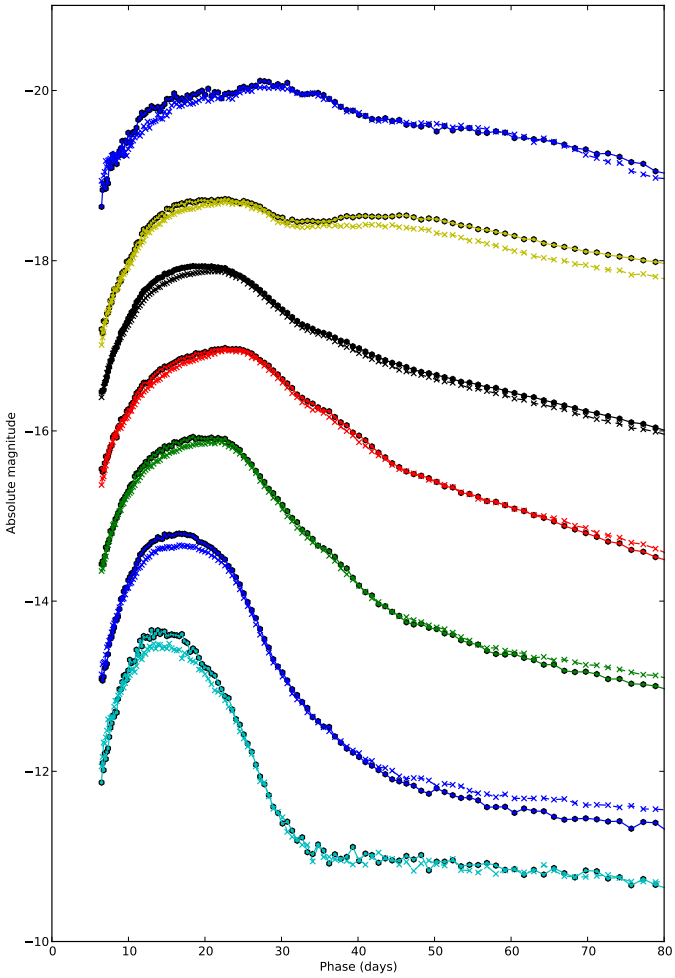

Fig. 2. Comparison of broadband and bolometric lightcurves for model 12C as calculated with JEKYLL (solid lines and circles) and ARTIS (dashed lines and crosses). From bottom to top we show the U **(cyan)**, B (blue), V (green), R (red), bolometric (black), I (yellow) and J (blue) lightcurves, which for clarity have been shifted with 2.0, 2.0, 1.5, 0.5, -1.0, -1.0 and -3.0 mags, respectively

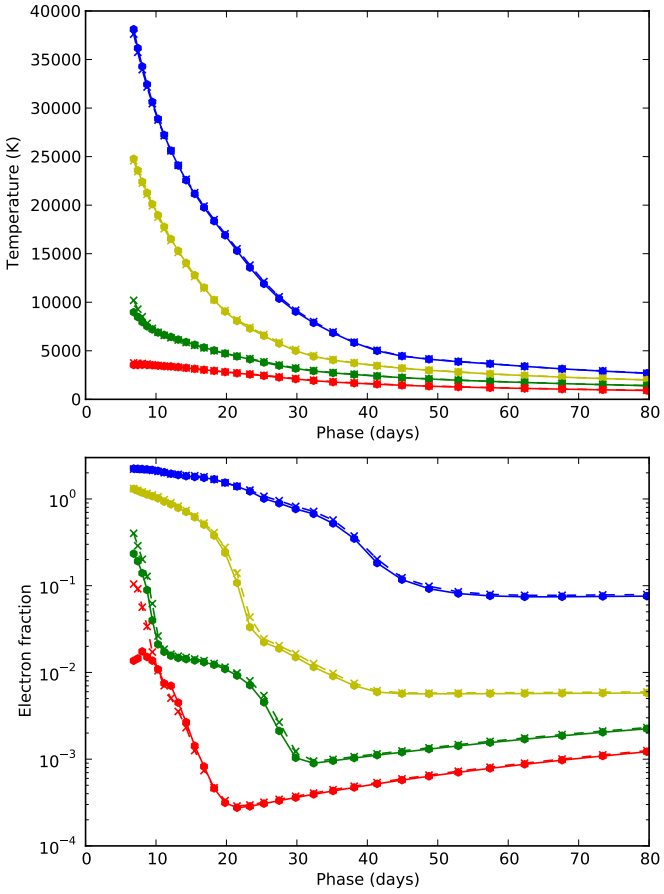

Fig. 3. Comparison of the evolution of the temperature (upper panel) and electron fraction (lower panel) in the oxygen core (blue), inner/outer (yellow/green) helium envelope and the hydrogen envelope (red) for model 12C as calculated with JEKYLL (circles and solid lines) and ARTIS (crosses and dashed lines).

plified NLTE treatment[1] where the excited states are populated according to LTE and the energy deposited by the radioactive decays goes solely into heating. On the other hand, JEKYLL assumes a spherical symmetric geometry, which is not a limitation in ARTIS. In addition, ARTIS calculates the deposition of the radioactive decay energy by Compton scattering, photoelectric absorption and pair production, whereas JEKYLL uses effective grey opacities (based on such calculations). There is also differences in the NLTE ionization treatment, in particular with respect to the calculation of photo-ionization rates, and due to this we decided to **run ARTIS** in its LTE mode. This still allows for a complete test of the time-dependent MC radiative transfer, which is the main purpose of the ARTIS comparison.

For the comparison we use the Type IIb model 12C from J15, which is also used in the application to Type IIb SNe (Sect. 5). **The model was converted to microscopically mixed form by averaging the abundances and then resampled to a finer grid.** To synchronize JEKYLL with ARTIS, it was was configured to run in time-dependent **(radiative transfer)** mode using the LTE solver, and the ARTIS atomic data was automatically converted to the JEKYLL format. The details of the code configurations and the atomic data used are given in Appendix A, and we find the synchronization good enough for a meaningful comparison. Note that as non-thermal processes are crucial for the population of the excited He I states, the characteristic He I signature of Type IIb SNe is not reproduced.

In Figs. 1 and 2 we compare the spectral evolution and the lightcurves, respectively, whereas in Fig. 3 we compare the evolution of the temperature and the electron fraction. As can be seen, the general agreement is good in both the observed and the state quantities. The most conspicuous discrepancy appears in the Ca II 8498,8542,8662 Å line after ~40 days, and give rise to a ~15 percent discrepancy in the *I*-band lightcurve. Another discrepancy appears after ~50 days in the *B*-band, growing towards ~15 percent at 80 days. There is also a small (<5 percent) but clear difference in the bolometric tail luminosity, reflecting a similar difference in the radioactive energy deposition. The reason for this is the more approximate method used by JEKYLL, which may also explain the differences in the tail broad-band lightcurves. There **are** also minor differences in the diffusion peak lightcurves, most pronounced in the *U*- and *B*-bands, which could be related to the simplified (but different) treatment at high optical depths in ARTIS and JEKYLL (see Appendix A.1). Summarizing, although there are some minor differences in the

[1] **A more general NLTE treatment and the inclusion of non-thermal processes in ARTIS are currently under development.**

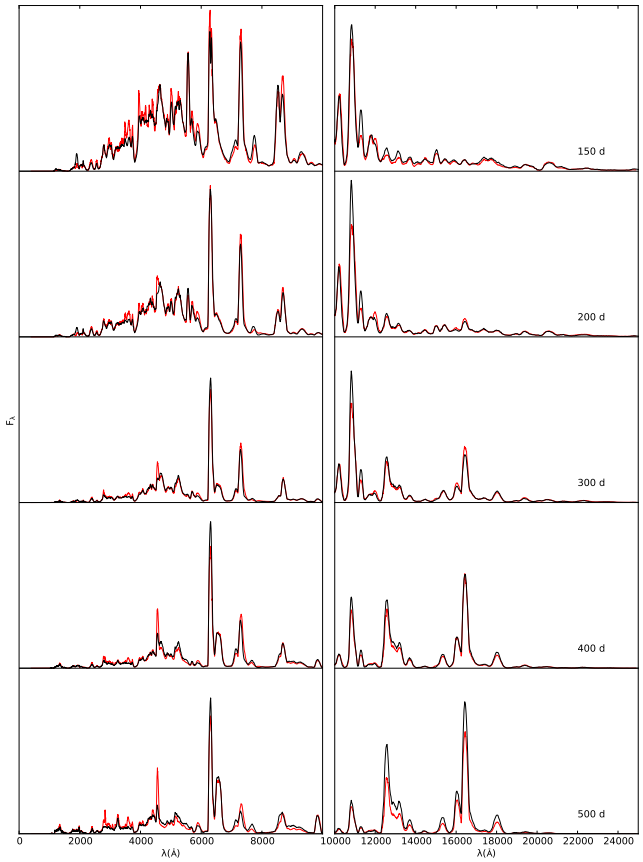

Fig. 4. Comparison of spectra for model 13G at 150, 200, 300, 400 and 500 days as calculated with JEKYLL (black) and SUMO (red).

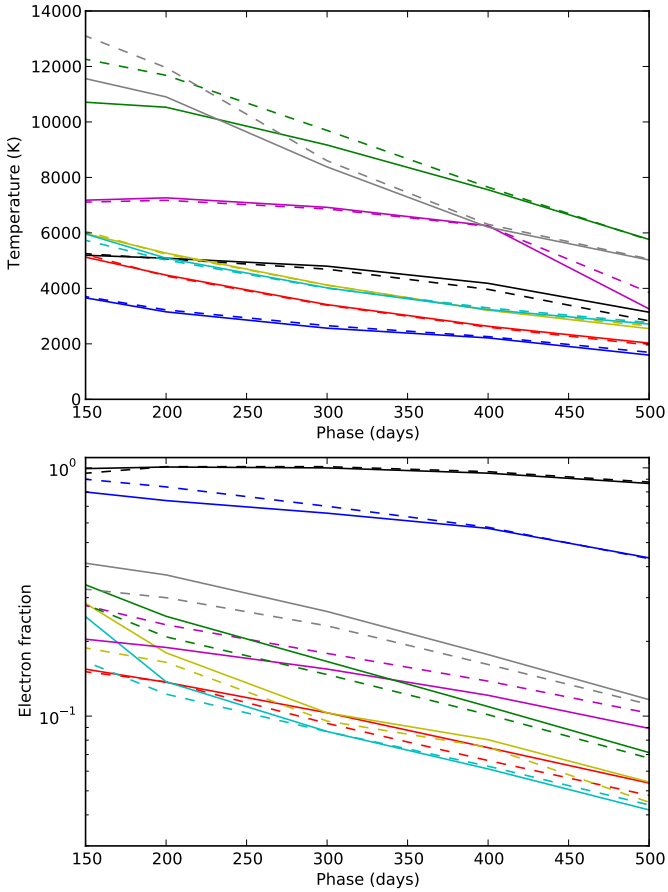

Fig. 5. Comparison of the evolution of the temperature (upper panel) and the electron fraction (lower panel) for model 13G in the **Fe/Co/He (black),** Si/S (blue), O/Si/S (red), O/Ne/Mg (yellow), O/C (cyan), He/C (magenta), He/N (green) and H (grey) zones as calculated with JEKYLL (solid lines) and SUMO (dashed lines).

spectra and the lightcurves, we find the overall agreement to be good.

4.2. Comparison with SUMO

SUMO is a spectral synthesis code aimed for the nebular phase presented in **J11 and J12**. Similar to JEKYLL, it uses a Λ-iteration scheme, where the radiative transfer is solved with a MC method and the state of the matter determined from statistical and thermal equilibrium. Except for the **(radiative transfer)** steady-state assumption, which is required by SUMO and an option in JEKYLL, the main difference between SUMO and JEKYLL is the MC technique used. Whereas JEKYLL is based on the method by L02-L05, where conservation of packet energy is enforced, SUMO uses another approach. Except for electron scattering and excitations to high lying states, the packet energy absorbed in free-free, bound-free and bound-bound processes is not re-emitted. As long as these processes are included in the emissivity from which the packets are sampled, this gives the correct solution in the limit of convergence. However, it could be **an issue** for the rate of convergence, in particular at high absorption depths, and the method is probably not suited for the photospheric phase. There are also a few differences in the physical assumptions. Whereas JEKYLL correctly samples the frequency dependence of the bound-free emissivity, this is done in a simplified manner for all species but hydrogen by SUMO. On the other hand, JEKYLL does not take the escape probability from continua and other lines in the Sobolev resonance region into account. However, in general the physical assumptions are similar.

For the comparison we use the Type IIb model 13G from J15, and run models with JEKYLL at 150, 200, 300, 400 and 500 days. To synchronize **JEKYLL** with SUMO, it was configured to run in steady-state mode using the NLTE solver, and we have tried to synchronize the atomic data as much as possible. The details of the code configurations and the atomic data used are given in Appendix A, and although not complete, we find the synchronization good enough for a meaningful comparison.

A comparison of the spectral evolution is shown in Fig. 4, and in Fig. 5 we compare the evolution of the temperature and the electron fraction in each of the different nuclear burning zones (see J15 and Sect. 5.1). As can be seen, the general agreement of the spectra is quite good, although the match is slightly worse at 500 days. The largest discrepancies are seen in the Mg I] 4571 Å line, the O I 11290,11300 Å line before 300 days, the He I 10830 Å line at 200-300 days, and a number of features originating from the Fe/Co/He zone at 500 days. That one of the largest discrepancies is seen in the Mg I] 4571 Å line is not surprising as magnesium is mainly ionized and the Mg I fraction is small (see J15). This makes the strength of the Mg I] 4571 Å line sensitive to this fraction, in turn sensitive to the network of charge transfer reactions.

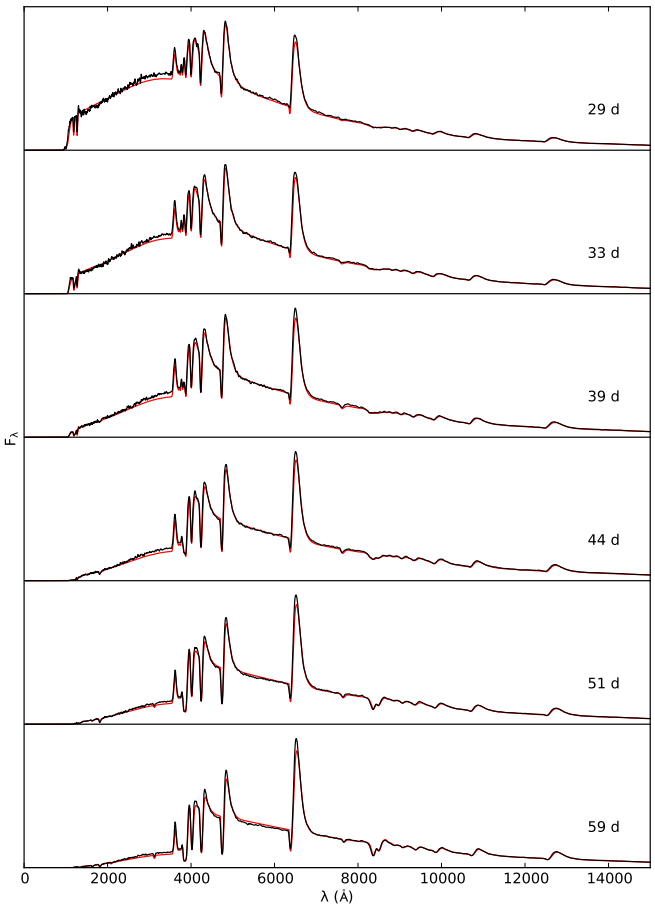

Fig. 6. Comparison of spectral evolution for the test model as calculated with JEKYLL (black) and CMFGEN (red).

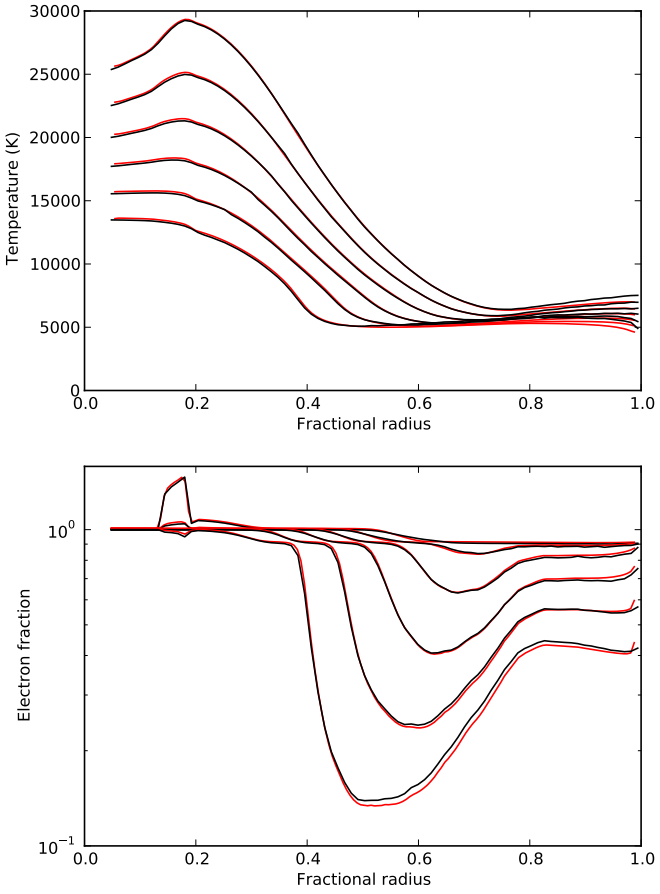

Fig. 7. Comparison of the evolution of the temperature (upper panel) and electron fraction (lower panel) at the same epochs as in Fig. 6 for the test model as calculated with JEKYLL (black) and CMFGEN (red).

The evolution of the temperature shows a good agreement and the differences are mainly below ∼5 percent. An exception is the He/N and H zones at early times, and in particular at 150 days where the difference is ∼15 percent. The evolution of the electron fraction shows a worse agreement, but the differences are mainly below ∼10 percent. Again, the agreement is worst at early times, and in particular at 150 days when the electron fractions in the O/Ne/Mg and O/C zones differ by ∼30 percent. This discrepancy is reflected in e.g. the O I 11290,11300 Å line discussed above, but in general the spectral agreement at 150 days is quite good. Summarizing, although there are some notable differences both in the spectra and the state variables, we find the overall agreement to be good, in particular as the data and the methods are not entirely synchronized.

4.3. *Comparison with CMFGEN*

CMFGEN is a general purpose spectral synthesis code presented in its steady-state version in H98, and extended with time-dependence in Dessart & Hillier (2008, 2010) and Hillier & Dessart (2012) and non-thermal processes in Dessart et al. (2012). It is similar to JEKYLL in the physical assumptions, but use a different method to solve the NLTE problem, where the coupled system of differential equations for the matter and the radiation field is solved by a linearization technique. The potential difficulties with convergence in Λ-iteration based methods (Sect. 2.1) are therefore avoided, and the comparison provides a good test of the convergence properties of the Λ-iteration and MC based method used in JEKYLL. The main difference in physical assumptions is that JEKYLL assumes steady state for the matter, wheras CMFGEN does not. In addition, CMFGEN does not rely on the Sobolev approximation, but this is likely of less importance at the high velocity gradients present in SNe ejecta.

For the comparison we use a model of a red supergiant of 15 $M_\odot$ initial mass, evolved with MESA (Paxton et al. 2011, 2013) and exploded with an energy of 1 Bethe with the hydrodynamical code HYDE (E14). The JEKYLL and CMFGEN simulations begin at 25 days, and for the test we use a highly simplified composition consisting of hydrogen, helium, oxygen and calcium. As it turned out to be difficult to switch the time-dependence off in CMFGEN in a self-consistent way, we instead added an option in JEKYLL to use the time-dependent NLTE rate equations. This is achieved by adding the time-derivative

$$\rho \frac{D(n_{I,j}/\rho)}{Dt} \tag{4}$$

to the right-hand side of Eq. 1 (see Dessart & Hillier 2008). This accounts for the effect of time-dependence on the degree of ionization, which is the most important one, at least in the test model. Note that time-dependence is only added in this limitied form to facilitate the comparison with CMFGEN, and is not explored further in the paper. A general upgrade of JEKYLL to full time-dependence will be presented in a forth-coming paper.

A comparison of the spectral evolution is shown in Fig. 6 and in Fig. 7 we compare the evolution of the temperature and the electron fraction. As can be seen, the overall agreement is good in both the spectra and the matter quantities. The largest differences in the spectra are a somewhat higher flux in the Balmer continuum and a bit stronger emission in the Balmer lines in the JEKYLL model. The electron fraction is in good agreement, but the temperature is slightly higher in the outer region in the JEKYLL model. Given that time-dependence is only partly implemented in JEKYLL, and is missing in the thermal energy equation, differences at this minor level is not surprising. The good overall agreement found in both the spectra and the matter quantities shows that the Λ-iteration and MC based method used in JEKYLL does indeed converge to the correct solution. Departures from LTE are large (typically a factor of ten or larger) in the optically thin region, so although based on a simplified model, the comparison provides a good test of the time-dependent NLTE capabilities. Comparisons between MC-based and traditional methods are very interesting, and we are planning to present more in-depth comparisons in a forthcoming paper.

5. Application to Type IIb SNe

In J15 a set of Type IIb models differing in initial mass and mixing (as well as other parameters; see J15) were introduced and evolved through the nebular phase. Among those, model 12C[2], which has an initial mass of 12 $M_\odot$ and strong mixing was found to give the best match to the observed nebular spectra (J15) and lightcurves (E15) of SN 2011dh. It is therefore of great interest to explore how well this model reproduces the early spectra and lightcurves, something which is now possible using JEKYLL. The early bolometric lightcurve was modelled in E15 using the hydrodynamical, LTE-based code HYDE[3], and we can now investigate how well this simplified approach compares with a full NLTE calculation. It is also worth comparing to the NLTE models of stripped envelope (SE; Type IIb, Ib and Ic) SNe presented by Dessart et al. (2015, 2016). Those models were evolved with CMFGEN and in particular the Type IIb model 3p65Ax1 shares many properties with model **12C**.

In Sect. 5.1 we describe the basic properties of the model and in Sects. 5.2, 5.3, 5.4 and 5.5 we discuss its spectral, photometric, colour and bolometric evolution and compare to observations of SN 2011dh. We also discuss the physical processes giving rise to the observed evolution and in Figs. 8 we show the evolution of the temperature, electron fraction, radioactive energy deposition and photosphere in model 12C. Finally, in Sects. 5.6 and 5.7 we discuss the effects of NLTE and macroscopic mixing on the calculated spectra and lightcurves.

5.1. Model description

A full description of model 12C is given in J15, but we repeat the basic properties here. It is based on a model by Woosley & Heger (2007) with an initial mass of 12 $M_\odot$, from which we take the masses and abundances for the carbon-oxygen core and the helium envelope. We assume the carbon-oxygen core to have a constant **(average)** density, and the helium envelope to have the same density profile as the best-fit model for SN 2011dh by Bersten et al. (2012). In addition, a 0.1 $M_\odot$ hydrogen envelope based on models by Woosley et al. (1994) is attached. The velocities of the interfaces between the carbon-oxygen core, the helium envelope and the hydrogen envelope are set to 3500 and 11000 km s^{-1}, respectively, based on observations of SN 2011dh.

Based on the original onion-like nuclear burning structure, five compositional zones (O/C, O/Ne/Mg, O/Si/S, Si/S and Fe/Co/He) are identified in the carbon-oxygen core, and two compositional zones (He/N and He/C) are identified in the helium envelope. To mimic the mixing of the nuclear burning zones in the explosion, two scenarios with different degrees of mixing (medium and strong) were explored in J15. The strong mixing scenario used for model 12C corresponds to a fully mixed carbon-oxygen core and about half of the radioactive Fe/Co/He material mixed into the inner part of the helium envelope. As in J15 we take the macroscopic nature of the mixing into account using the virtual cell method (Sect. 3.1.2). **However, here we use this method also in the helium envelope, where J15 used alternating shells to represent the mixing.** We have also run a model with microscopic mixing by just averaging the abundances, and the difference is discussed in Sect. 5.7.

JEKYLL was configured to run in time-dependent **(radiative transfer) mode using the NLTE solver based on** an updated version of the J15 atomic data, and we give the details of the configuration and the atomic data in Appendix A. The model was evolved from 1 to 150 days, and as for the HYDE models in E15, the initial temperature profile was taken from the best-fit hydrodynamical model for SN 2011dh from that paper. This SN model was based on a bare helium core model, and therefore the cooling of the thermal explosion energy, lasting for a few days in a model with a hydrogen envelope, is ignored. The subsequent evolution is powered by the continuous injection of radioactive decay energy, and the choice of initial temperature profile is not critical, although it may have some effect on the early evolution.

5.2. Spectral evolution

Figures 9 and 10 show the spectral evolution for model 12C between 0 and 150 days, where the former **figure** displays the process, and the latter **figure** the location giving rise to the emission[4]. Furthermore, in Fig. 11 we compare the spectral evolution in the optical and near-infrared (NIR) to observations of SN 2011dh. As seen in Fig. 11, there is a good qualitative, and in many aspects also quantitative agreement, between model 12C and the observations of SN 2011dh. Before ∼10 days, when the emission comes mainly from the hydrogen envelope the agreement is a bit worse (not shown). This is possibly an effect of the choice of initial conditions for the model (see Sect. 5.1), where the initial cooling of the explosion energy, lasting a few days, has been ignored.

The main signature of a Type IIb SN is the transition from a hydrogen to a helium dominated spectrum, and this is well reproduced by the model. Initially, the hydrogen lines are strong and emission from the hydrogen envelope is dominating. Already at ∼10 days emission from the helium envelope starts to dominate redwards ∼5000 Å, and between 10 and 15 days the helium lines appear, grow stronger, and eventually dominate the spectrum at ∼40 days. Hydrogen line emission disappears on a similar time-scale, completing the transition, although the Balmer lines remain considerably longer in absorption. The first 40 days

[2] Model 12F, preferred in E15, differs from model 12C only in the optical depth of the dust.

[3] Set up to run in homologous mode

[4] Based on the last emission events for the MC packets excluding electron scattering.

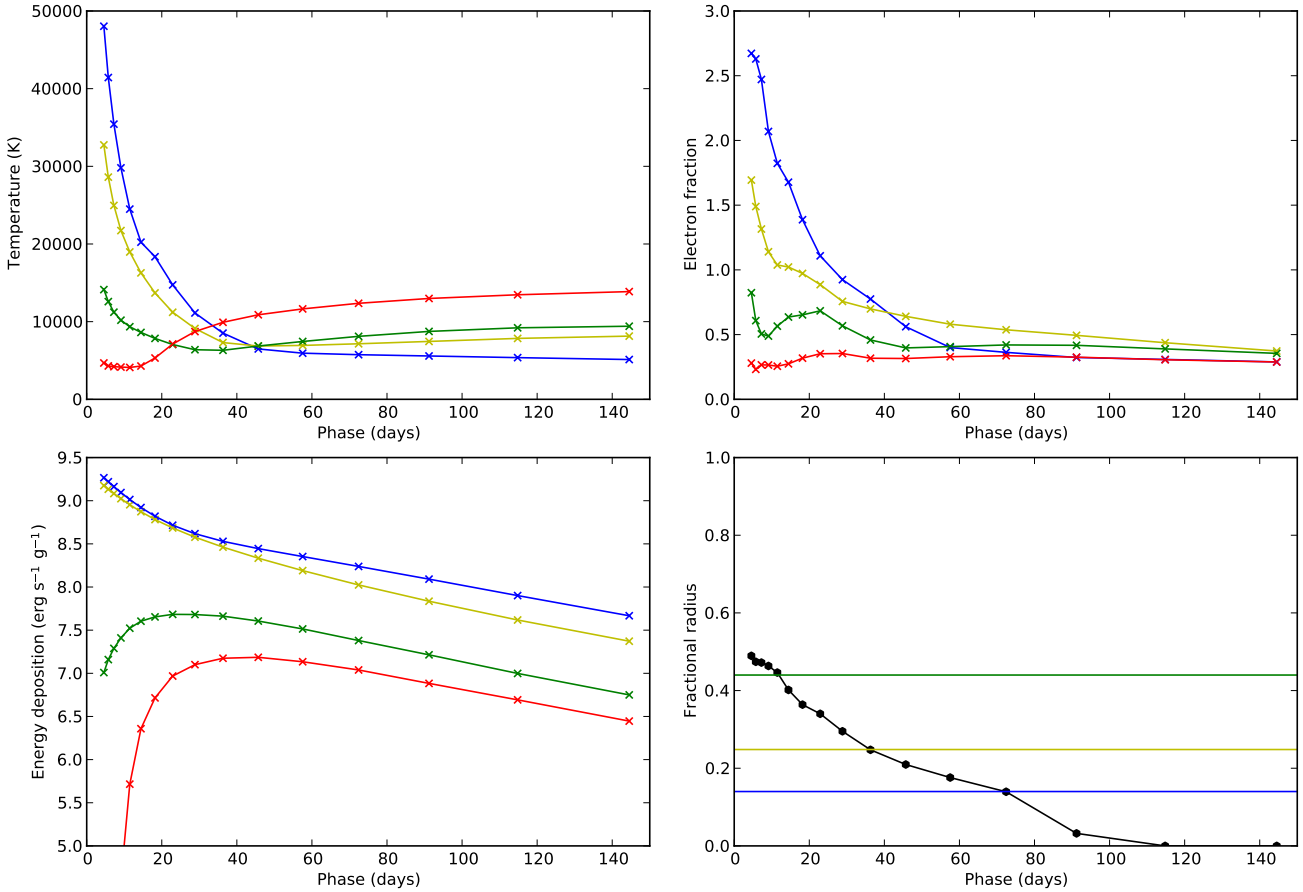

Fig. 8. Evolution of the temperature (upper left panel), electron fraction (upper right panel) and radioactive energy deposition (lower left panel) in the oxygen core (blue), inner/outer (yellow/green) helium envelope and the hydrogen envelope (red) for model 12C. In the lower right panel we show the evolution of the (Rosseland mean) continuum photosphere as well as the outer borders of the carbon-oxygen core (blue) and inner/outer (green/yellow) helium envelope.

is also the period over which the contribution from continuum processes fades away. Initially, this contribution is substantial redwards ~5000 Å and dominating in the NIR, but then quickly fades away although it remains important in the *H*-band and redwards 23000 Å until ~40 days.

After ~40 days, emission from the carbon-oxygen core becomes increasingly important and at ~100 days it dominates redwards ~5000 Å. As a consequence, emission from heavier elements abundant in the core increases, in particular after ~100 days, when the characteristic [O I] 6300,6364 Å and [Ca II] 7291,7323 Å lines appear. This is also the moment when the carbon-oxygen core becomes fully transparent in the continuum (see Fig.8), and therefore marks the transition into the nebular phase. This transition, in itself a demanding test of the code, is quite nicely reproduced by the model. As discussed in Sect. 5.7, this is partly due to our treatment of the macroscopic mixing.

Below, we discuss the most important lines originating from the different elements in some detail (Sects. 5.2.1-5.2.5) as well as the line velocities measured from their absorption minima (Sect. 5.2.6), and again compare to observations of SN 2011dh.

5.2.1. Hydrogen

The contribution from hydrogen lines is shown in Fig. 9, and as mentioned it is initially strong, but fades away after ~10 days, when the photosphere retreats into the increasingly transparent helium envelope (see Fig. 8). This trend is most pronounced for the recombination driven Paschen lines, which disappear towards ~40 days. Balmer line emission fades on a similar timescale, whereas absorption remains for a longer time, and even increases before ~40 days. Contrary to the other Balmer lines, Hα initially shows a clear P-Cygni profile, but after ~10 days it becomes increasingly blended with the He I 6678 Å line and attains the double-peaked shape so characteristic in Type IIb SNe.

Figure 12 shows the evolution of the Balmer lines as compared to SN 2011dh. The evolution is qualitatively similar, but the absorption is significantly stronger and remains longer in the model, suggesting that the ~0.05 $M_\odot$ of hydrogen in the model is larger than for SN 2011dh. This is in line with the 0.02-0.04 and 0.024 $M_\odot$ of hydrogen estimated through spectral modelling of SN 2011dh by E14[5] and Marion et al. (2013), respectively. In agreement with the spectral modelling in E14, we also find that the absorption minimum of the Balmer lines asymptotically approaches the velocity of the helium/hydrogen envelope interface. The Type IIb models by Dessart et al. (2015, 2016) behave in a similar way, and a saturation of the absorption velocity for the Balmer lines is observed in most Type IIb SNe (see e.g. Liu et al. 2016). The saturation velocity varies among different SNe,

[5] Using an early version of JEKYLL assuming steady-state, LTE and (electron and line) scattering only.

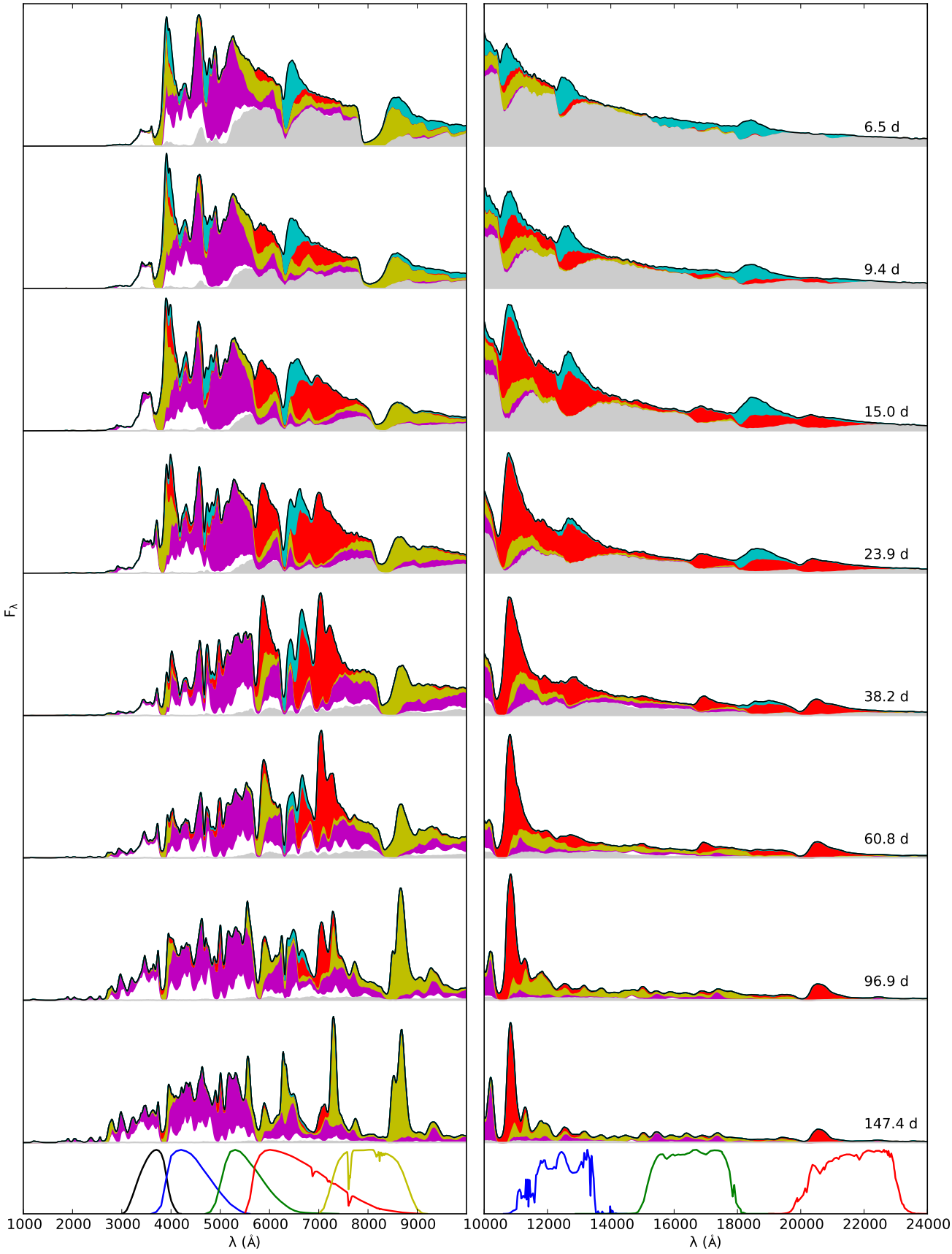

Fig. 9. Spectral evolution in the optical (left panel) and NIR (right panel) for model 12C as calculated with JEKYLL. In the spectra we show the contributions to the emission from bound-bound transitions of hydrogen (cyan), helium (red), carbon-calcium (yellow), scandium-manganese (white) and iron-nickel (magenta) as well as continuum processes (grey). At the bottom we show the transmission profiles of the optical Johnson-Cousins *U* (black), *B* (blue), *V* (green), *R* (red) and *I* (yellow) bands and the NIR 2MASS *J* (blue), *H* (green) and *K* (red) bands.

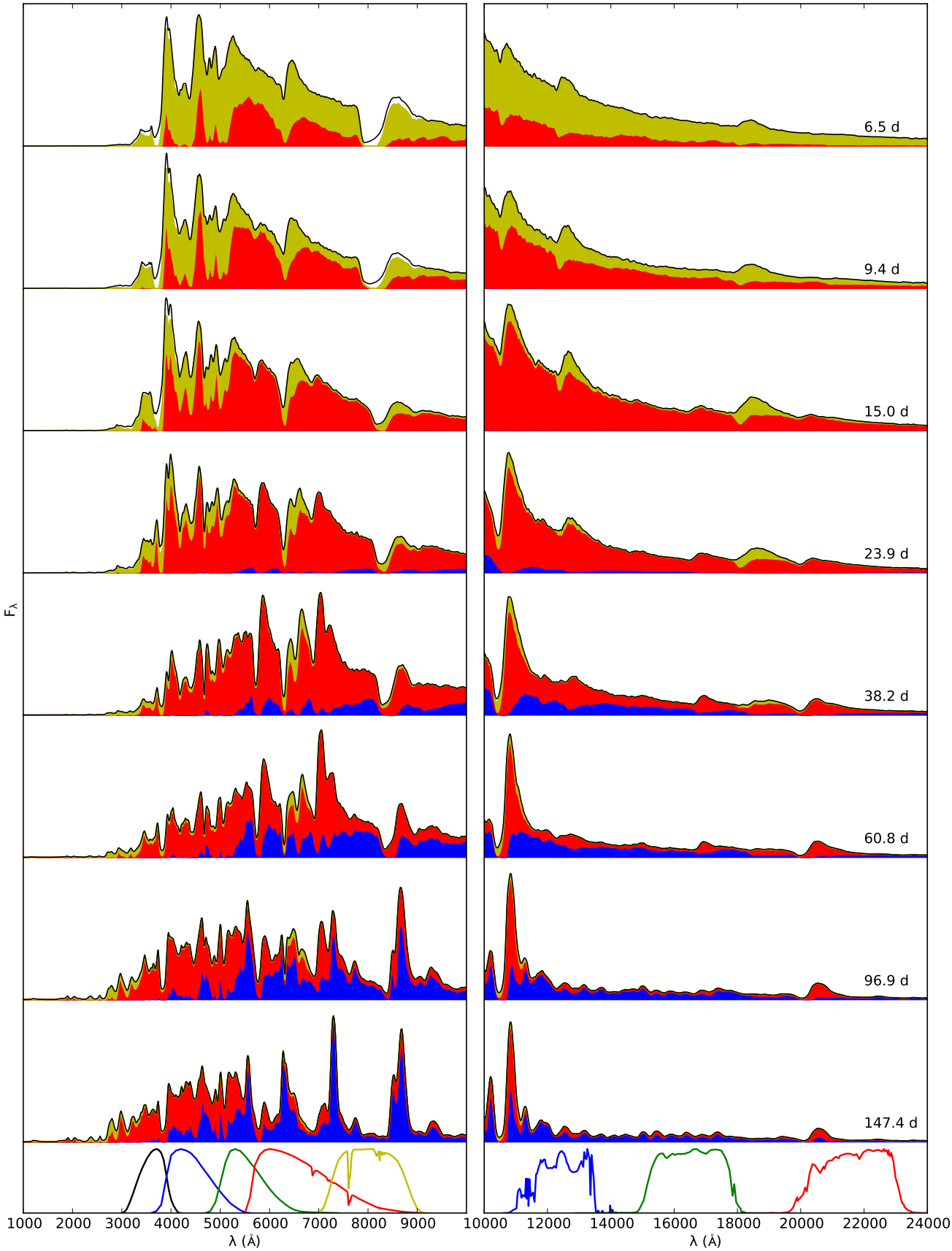

Fig. 10. Spectral evolution in the optical (left panel) and NIR (right panel) for model 12C as calculated with JEKYLL. In the spectra we show the contributions to the emission from the carbon-oxygen core (blue), and the helium (red) and hydrogen (yellow) envelopes. At the bottom we show the transmission profiles of the optical Johnson-Cousins *U* (black), *B* (blue), *V* (green), *R* (red) and *I* (yellow) bands and the NIR 2MASS *J* (blue), *H* (green) and *K* (red) bands.

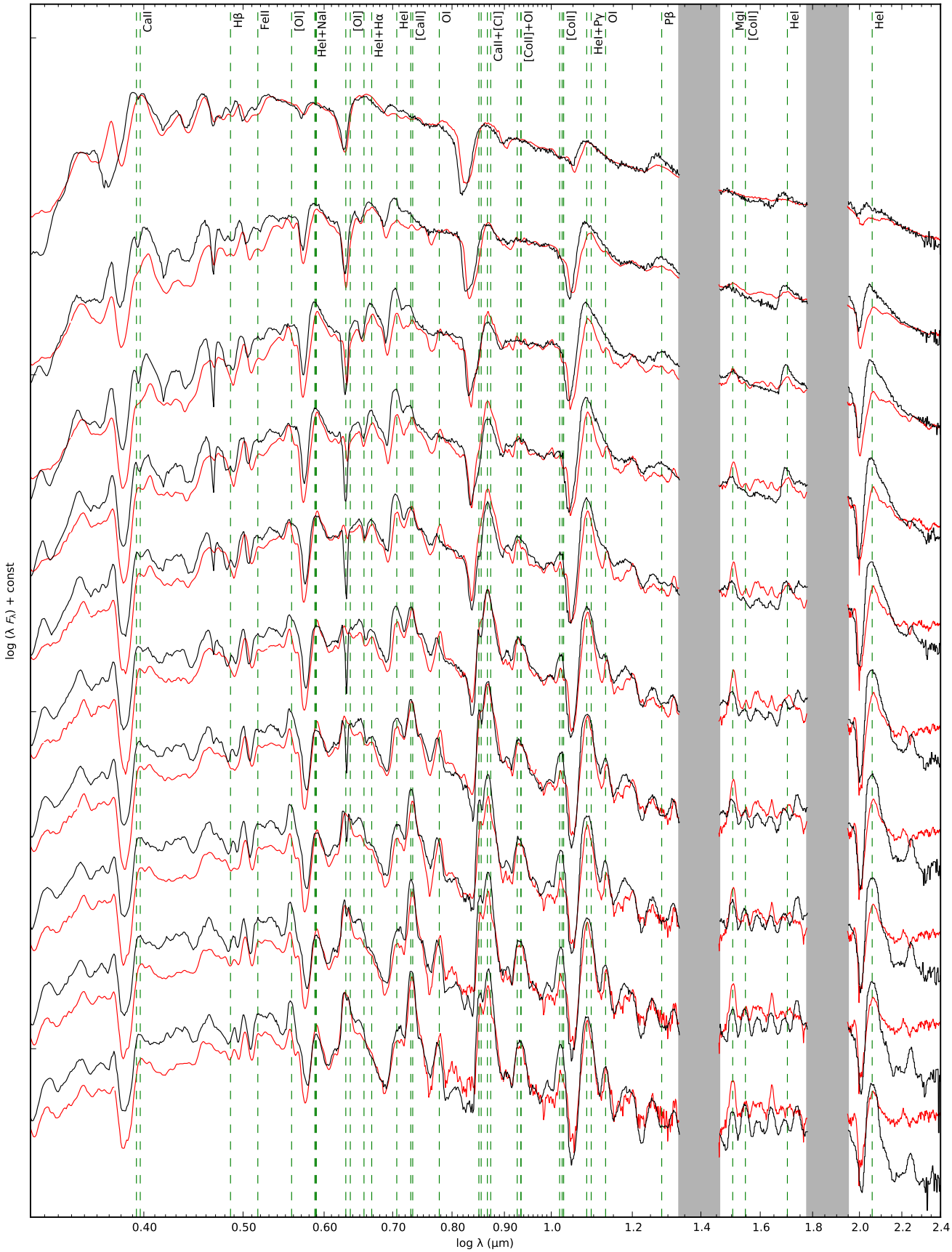

Fig. 11. Spectral evolution for model 12C as calculated with JEKYLL (black) compared to the observations of SN 2011dh (red). Spectra from 10 equally spaced epochs between 15 and 150 days are shown, where those of SN 2011dh have been interpolated as described in E14. **In addition, the rest-wavelengths of the most important lines are shown as red dashed lines and the NIR telluric absorption bands as grey vertical bars**.

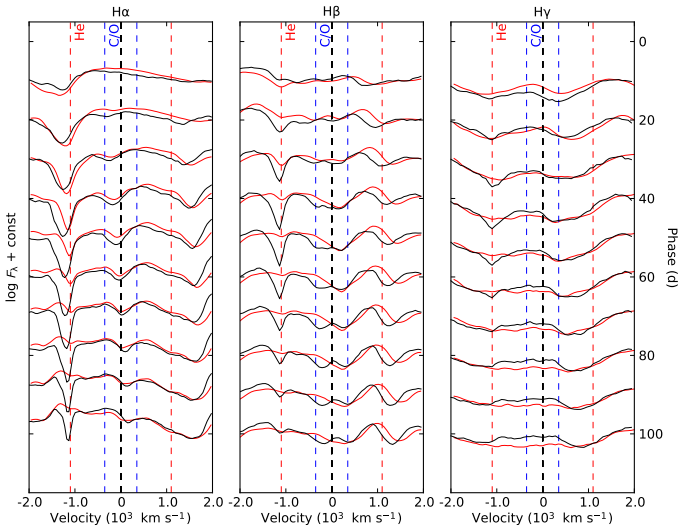

Fig. 12. Evolution of hydrogen lines for model 12C as calculated with **JEKYLL** (black) compared to the observations of SN 2011dh (red). Spectra from 10 equally spaced epochs between 10 and 100 days are shown, where those of SN 2011dh have been interpolated as described in E14. Here, as well as in Figs. 13-16, we also show the velocity extent of the helium envelope (red lines) and the carbon-oxygen core (blue lines).

and for the most well-observed Type IIb SNe 1993J, 2011dh and 2008ax it is ∼9000, ∼11000 and ∼13000 km s^{-1} respectively, suggesting progressively lower hydrogen masses for these SNe **(E14)**.

5.2.2. Helium

The contribution from helium lines is shown in Fig. 9, and as mentioned it increases strongly between 10 and 15 days, dominates the spectrum between 20 and 60 days and thereafter fades away in the optical but remains important in the NIR. As demonstrated by Lucy (1991), non-thermal excitation and ionization are essential to populate the excited levels of He I, in turn required to produce the lines observed. This was confirmed using CMFGEN by Dessart et al. (2012) and in Sect. 5.6 we explore the effect of non-thermal processes further. As pointed out by Lucy (1991), the population process is subtle, as ionization of He I is amplified by photo-ionization from the excited levels, which proceeds at a rate far exceeding the non-thermal one.

Figure 13 shows the evolution of the He I 5876 Å, 6678 Å, 7065 Å, 10830 Å, 17007 Å and 20581 Å lines as compared to SN 2011dh. These are the lines that stand out most clearly in the model, but several other weaker and blended lines are also present. The He I 5876 Å, 6678 Å and 10830 Å lines are quite well reproduced by the model, whereas the He I 7065 Å and 20581 Å lines are a bit overproduced, and the weaker He I 17007 Å line (mainly seen in emission) is considerably stronger than in the observed spectra. Note, that after ∼50 days most of the He I 5876 Å line emission begin to scatter into the Na I 5890,5896 Å line.

As seen in Fig. 13, the He I 10830 Å absorption migrates outward in velocity until ∼40 days, a behaviour repeated to some degree in the He I 20581 Å line. This behaviour is also observed in SN 2011dh, although in that case the optical helium lines showed a similar, but less pronounced trend. In E14 we suggested that the evolution of the helium lines is driven mainly

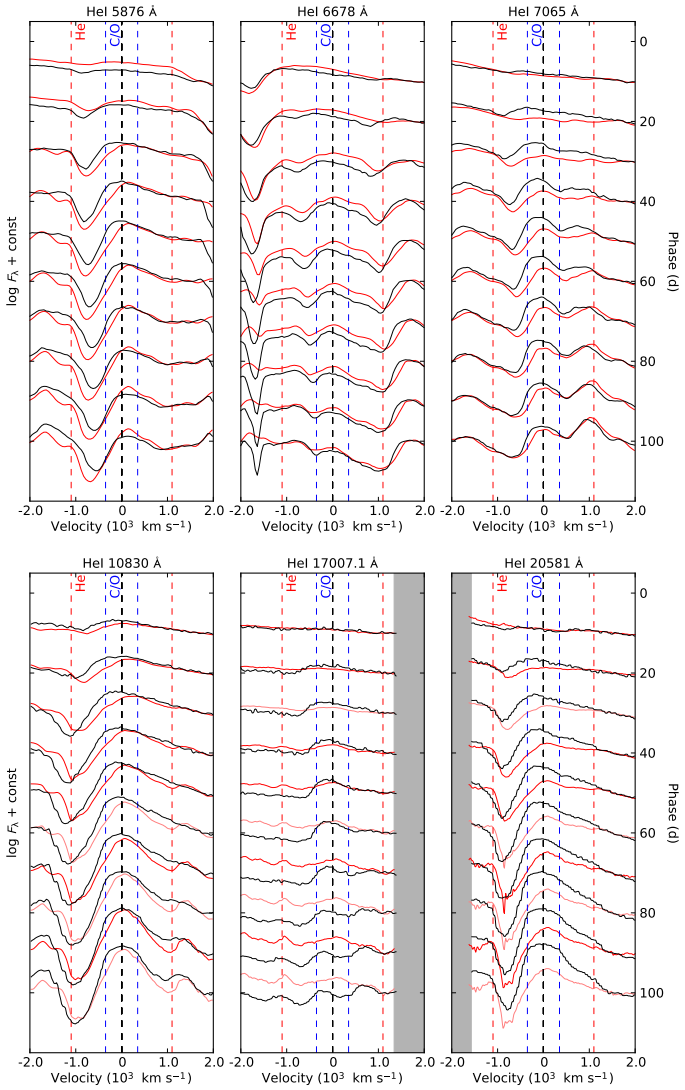

Fig. 13. Evolution of optical (upper panel) and NIR (lower panel) helium lines for model 12C as calculated with **JEKYLL** (black) compared to the observations of SN 2011dh (red). Spectra from 10 equally spaced epochs between 10 and 100 days are shown, where those of SN 2011dh have been interpolated as described in E14.

by the ejecta becoming optically thin to the γ-rays. This idea is supported by Fig. 14, which shows the evolution of the radioactive energy deposition in the helium envelope. Between 10 and 15 days we see a strong increase in the energy deposition outside the photosphere, corresponding well to the period when the helium lines appear and grow in strength. We also see that the energy deposition in the outermost helium layers continues to increase to ∼40 days, which may explain the evolution of the He I 10830 Å line. The outward migration of the He I 10830 Å absorption is also present in the Type I/IIb models (e.g. model 3p65Ax1) by Dessart et al. (2015, 2016), and was noted and discussed by the authors, who also provide a similar explanation.

5.2.3. Carbon-calcium

The (line) contribution from elements in the carbon-calcium range is shown in Fig. 9, and except for the calcium lines which are strong at all times, the contribution increases after ∼40 days

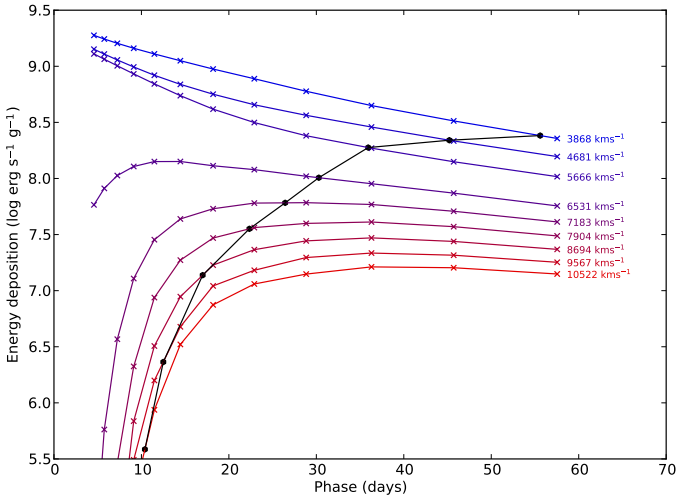

Fig. 14. Evolution of the radioactive energy deposition in the helium envelope (red to blue crosses) and the position of the (Rosseland) continuum photosphere (black circles) for model 12C .

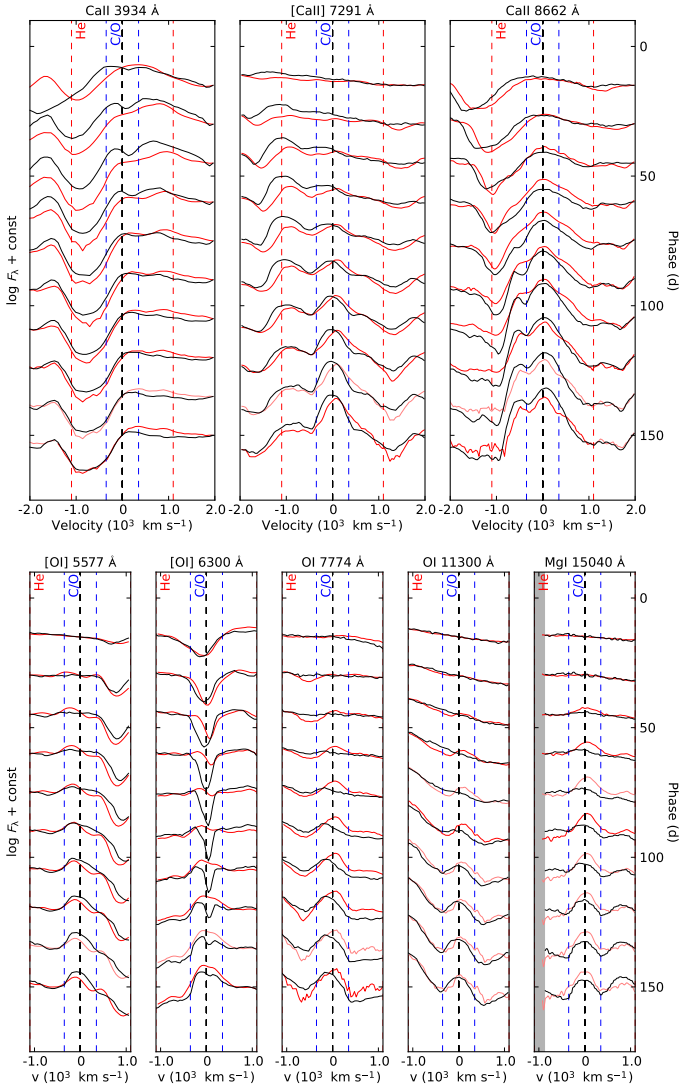

Fig. 15. Evolution of calcium, oxygen and magnesium lines for model 12C as calculated with **JEKYLL** (black) compared to the observations of SN 2011dh (red). Spectra from 10 equally spaced epochs between 15 and 150 days are shown, where those of SN 2011dh have been interpolated as described in E14.

when the core, rich in these elements becomes increasingly transparent (see Fig. 10). The upper panel of Fig. 15 shows the evolution of the Ca II 3934,3968 Å, Ca II 8498,8542,8662 Å and [Ca II] 7291,7323 Å lines as compared to SN 2011dh. After ~15 days the evolution of these lines is well reproduced by the model. However, at earlier times absorption in the Ca II 3934,3968 Å and Ca II 8498,8542,8662 Å lines extend further out in the model. Again, this is possibly an effect of the choice of initial conditions.

The lower panel of Fig. 15 shows the evolution of the [O I] 5577 Å, [O I] 6300,6364 Å, O I 7774 Å, O I 11290,11300 Å and Mg I 15040 Å lines as compared to SN 2011dh. The evolution of the oxygen lines is fairly well reproduced, but the O I 7774 Å and 11290,11300 Å lines appear later and are initially weaker than observed for SN 2011dh. The O I 9263 Å line is also present in the model but is blended with the [Co II] 9338,9344 Å line (see Sect. 5.2.5).

In the model, the early (near peak) feature at ~9200 Å is mainly caused by the Mg II 9218,9244 Å line, and later the Mg I 15040 Å line appears. The latter is well reproduced in the nebular phase (after ~100 days), but appears later and is initially weaker than observed for SN 2011dh. We note that whereas the radioactive Fe/Co/He material was mixed into the helium envelope, the oxygen and magnesium rich material was not, which may explain the early suppression of several oxygen and magnesium lines as compared to observations.

As mentioned in Sect. 5.2.2, the Na I 5890,5896 Å line overtakes He I 5876 Å line at ~60 days, and as seen in Fig. 13 the subsequent evolution is well reproduced. In the model, the feature emerging at ~11800 Å after ~60 days is mainly caused by the C I 11760 Å line, and towards ~150 days the [C I] 8727 Å line begins to contribute significantly to the blend with the Ca II 8498,8542,8662 Å line.

5.2.4. Scandium-manganese

The (line) contribution from elements in the scandium-manganese range is shown in Fig. 9, and is dominating in the 3000-4000 Å region and important in the 4000-5000 Å region at all times. After ~40 days it also contributes significantly to the optical emission redwards 5000 Å. The emission is the result of scattering and fluorescence in numerous transitions and individual lines are hard to distinguish. Line-blocking by elements in the scandium-manganese range is important for the suppression of the emission bluewards ~5000 Å, and in particular in the 3000-4000 Å region, corresponding roughly to the *U*-band.

5.2.5. Iron-nickel

The (line) contribution from elements in the iron-nickel range is shown in Fig. 9, and this contribution is strong at all times, in particular in the 4000-5500 Å range. After ~40 days the contribution increases also at other wavelengths, likely due to emission from the increasingly transparent core (see Fig. 10), where about half of the Fe/Co/He material resides. Except for the *U*-band (see Sect. 5.2.4), blocking through scattering and fluorescence in numerous iron lines is the main cause for the suppression of the

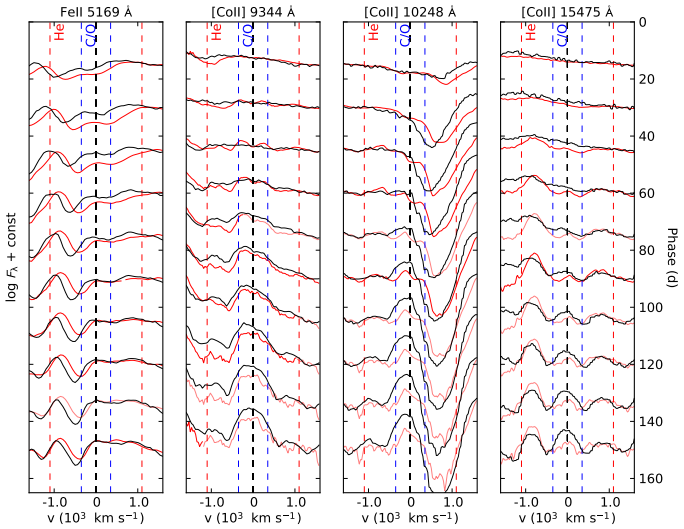

Fig. 16. Evolution of iron and cobalt lines for model 12C as calculated with **JEKYLL** (black) compared to the observations of SN 2011dh (red). Otherwise as in Fig. 15.

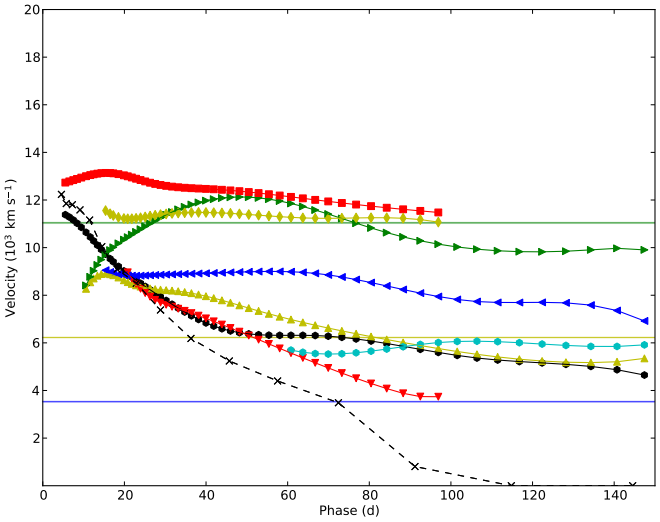

Fig. 17. Velocity evolution of the absorption minimum of the Hα (red squares), Hβ (yellow diamonds), He I 5876 Å (yellow upward triangles), He I 6678 Å (red downward triangles), He I 10830 Å (green rightward triangles), He I 20581 Å (blue leftward triangles), O I 7774 Å (cyan circles) and Fe II 5169 Å (black circles) lines for model 12C as calculated with JEKYLL. The black crosses show the velocity evolution of the (Rosseland mean) continuum photosphere, whereas the horizontal lines mark the outer borders of the carbon-oxygen core (blue) and inner/outer (green/yellow) helium envelope.

emission bluewards ~5500 Å, so important in shaping the spectra of SE SNe. However, with a few exceptions, like the Fe II 5169 Å line, individual iron lines are typically strongly blended and hard to distinguish. The contribution from nickel is insignificant at all times, but after ~50 days cobalt begins to contribute to the spectrum with several distinct lines.

Figure 16 shows the evolution of the Fe II 5169 Å and [Co II] 9338,9344 Å, [Co II] 10190,10248,10283 Å and [Co II] 15475 Å lines as compared to SN 2011dh. The Fe II 5169 Å line is reasonably well reproduced, but initially absorption occurs at higher velocities than observed, a discrepancy that disappears towards 150 days. As mentioned the [Co II] 9338,9344 Å line is blended with the O I 9338,9344 Å line, and this blend is well reproduced by the model. The other [Co II] lines at 10190,10248,10283 Å and 15475 Å are a bit overproduced by the model. The iron and cobalt lines are interesting as they are directly linked to the distribution of the Fe/Co/He material in the ejecta, and the discrepancies seen may indicate that the mixing of this material is different than in the model.

5.2.6. Line velocities

Figure 17 shows the velocity evolution of the absorption minima of the Hα, Hβ, He I 5876 Å, He I 6678 Å, He I 10830 Å, He I 20581 Å, O I 7774 Å and Fe II 5169 Å lines, as well as the (Rosseland mean) continuum photosphere (compare; E15: Fig. 14). The hydrogen lines show the highest velocities, have a flat evolution, and as discussed (Sect. 5.2.1), they approach the velocity of the interface between the helium and hydrogen envelopes. The evolution is mostly in agreement with observations, but the high Hα velocities observed before ~10 days for SN 2011dh are not reproduced by the model, which could again be related to our choice of initial **conditions.** The helium lines appear between 10 and 15 days near the photosphere and then evolve quite differently, where the He I 10830 Å velocity increases towards that of Hα, the He I 20581 Å velocity stays almost flat, and the He I 5876 Å and 6678 Å velocities decline. The evolution of the He I 10830 Å and 20581 Å velocities is in quite good agreement with observations, whereas the He I 5876 Å and 6678 Å velocities differ more.

As discussed (Sect. 5.2.3), the O I 7774 Å line appears later than in SN 2011dh, but the velocity evolution is otherwise similar, being rather flat at ~6000 km/s. The evolution of the Fe II 5169 Å velocity follows that of the (Rosseland mean) continuum photosphere until ~30 days, confirming the common assumption (e.g. E14) that this line is a good tracer of the photosphere during the diffusion phase. However, as mentioned before, this velocity is higher than observed for SN 2011dh, although the discrepancy disappears towards 150 days (see Fig. 16). It is worth noting that the Fe II 5169 Å velocity reaches a plateau near ~6000 km s^{-1} at ~40 days, a value close to the outer border of the inner helium envelope. This is **a** hint that the amount of Fe/Co/He material mixed into this part of the helium envelope could be too large, which in turn could force the photosphere to too high velocities.

5.3. Photometric evolution

Figure 18 shows the broad-band lightcurves for model 12C between 0 and 150 days as compared to observations of SN 2011dh. In agreement with observations, the maximum occurs at increasingly later times for redder bands and the drop onto the tail is more pronounced (deeper and faster) for bluer bands. Also in agreement with observations, the early (before 100 days) tail decline rates are generally higher for redder bands, with the *J*-band lightcurve having the steepest slope and the *U*-band lightcurve being almost flat. As **has** been noted in several sample studies (e.g. Taddia et al. 2015, 2017), the aforementioned behaviour of the maxima and the subsequent decline is shared not only by SN 2011dh, but by SE-SNe in general. It is also in agreement with the SE-SNe NLTE models presented by Dessart et al. (2015, 2016), and the lightcurves of the Type IIb model 3p65Ax1 are particularly similar to those of model 12 C.

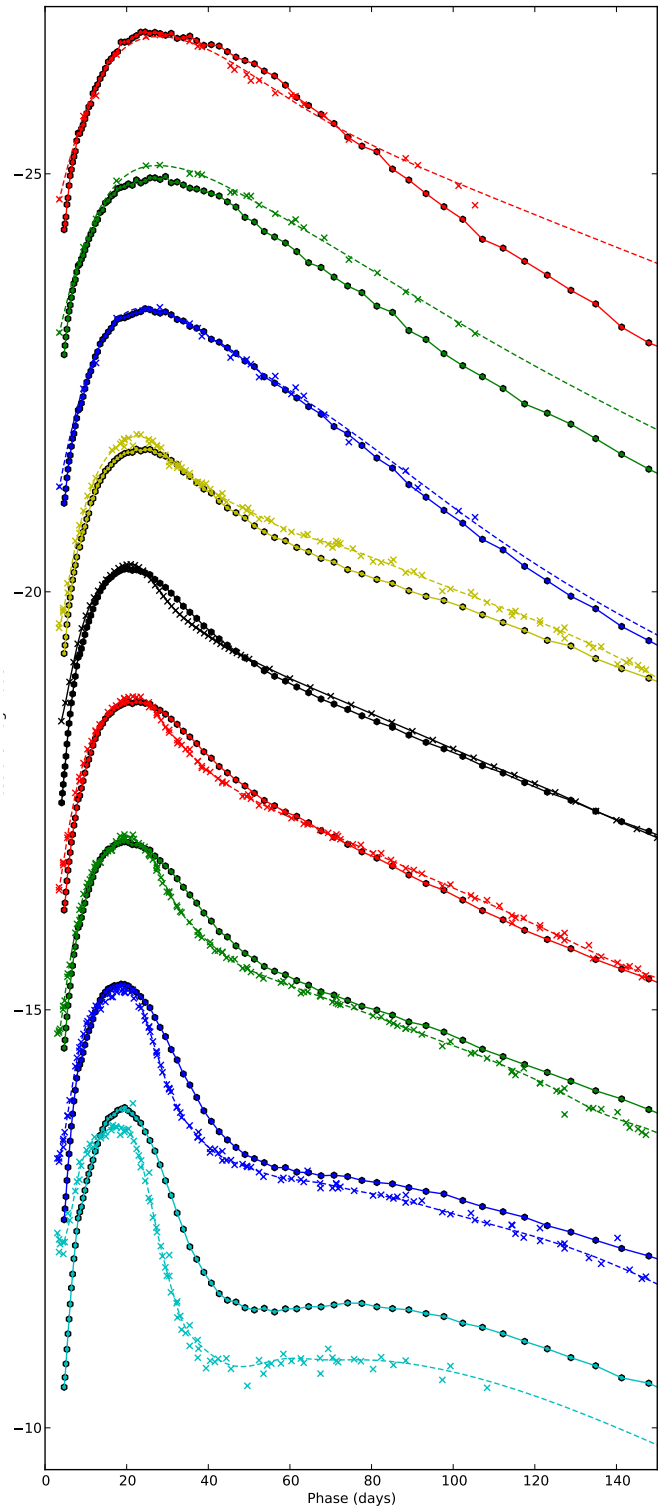

Fig. 18. Broadband and bolometric lightcurves for model 12C as calculated with JEKYLL (solid lines and circles) compared to observations of SN 2011dh (dashed lines and crosses). From bottom to top we show the U **(cyan)**, B (blue), V (green), R (red), UV to MIR pseudo-bolometric (black), I (yellow), J (blue), H (green) and K (red) lightcurves, which for clarity have been shifted with 2.6, 1.2, 0.0, -1.4, -3.5, -4.4, -5.8, -7.5, -8.9 mags, respectively.

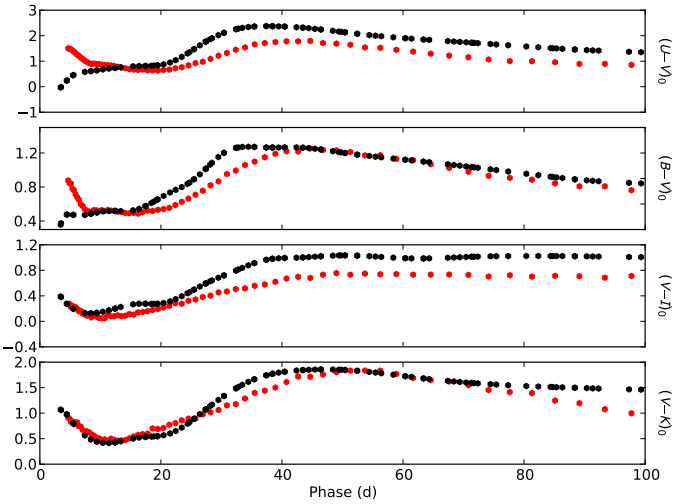

Fig. 19. $U-V$, $B-V$, $V-I$ and $V-K$ intrinsic colour evolution for model 12C as calculated with JEKYLL (black) compared to observations of SN 2011dh (red).

Although the overall agreement with observations is quite good, there are several differences between the model and the observations of SN 2011dh worth noting. Most notable are the differences in the U, J and K-bands and the evolution between 25 and 50 days, which is slower in R and bluer bands than observed for SN 2011dh. The growing discrepancy in the K-band could be related to dust formation in the ejecta (E15), and might suggest that this happens earlier than proposed in E15. Some of the discrepancy in the U-band could be explained by an underestimate of the extinction, but not all as the discrepancy is considerably larger on the tail than at peak.

5.4. Colour evolution

Figure 19 shows the intrinsic $U-V$, $B-V$, $V-I$ and $V-K$ colour evolution for model 12C between 0 and 100 days as compared to observations of SN 2011dh. Initially, we see a blueward trend in all colours reaching a minimum at ∼10 days. Subsequently all colours redden and **reach** a maximum at ∼40 days, in turn followed by a slow blueward trend for all colours, although the $V-I$ colour stays almost constant. This behaviour is in agreement with observations, although SN 2011dh does not show an initial blueward trend in the $U-V$ and $B-V$ colours, likely due to the influence of an initial cooling tail, not present in the model due to our choice of initial conditions.

As **has** been noted in several sample studies (e.g. Stritzinger et al. 2017), the properties of the colour evolution discussed here are shared not only by SN 2011dh, but by SE-SNe in general. They are also in agreement with the SE-SNe NLTE models presented by Dessart et al. (2015, 2016), and the colour evolution of the Type IIb model 3p65Ax1 is particularly similar to that of model 12 C. As was noted for the lightcurve, the model evolution after ∼20 days is a bit slower than observed for SN 2011dh. The model $V-I$ and $U-V$ colours are bluer than observed for SN 2011dh, reflecting differences in the I- and U-bands.

5.5. Bolometric evolution

Figure 18 shows the pseudo-bolometric UV to MIR lightcurve for model 12C between 0 and 150 days as compared to observations of SN 2011dh. Similar to the comparison of the broad-

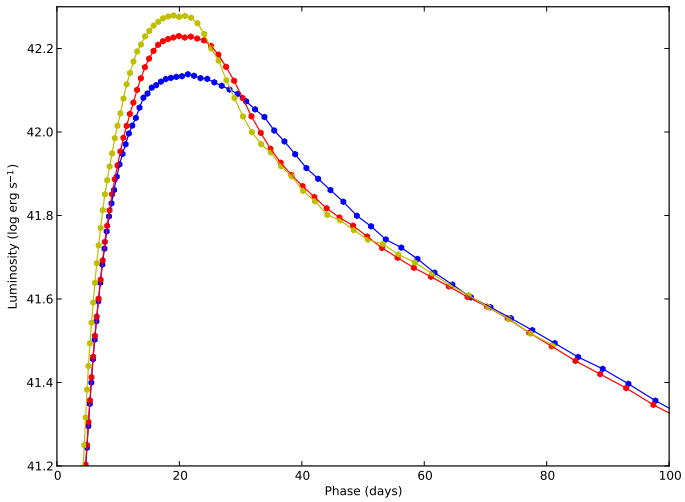

Fig. 20. Bolometric lightcurve for model 12C calculated with (blue) and without (red) non-thermal ionization and excitation. We also show a model assuming LTE for the excited levels (yellow), calculated in a manner similar to ARTIS.

band lightcurves, the model bolometric lightcurve is not a perfect match and is broader than the observed one. As the photospheric velocity is higher in the model (Sect. 5.2.6), this might indicate that a lower ejecta mass is needed. On the other hand, the mixing of the radioactive Fe/Co/He material plays a stronger role when non-thermal processes are taken into account (Sect. 5.6), and there are several indications (Sects. 5.2.3, 5.2.5 and 5.2.6) that the mixing may differ from that of SN 2011dh. We leave a further exploration of this, which would require a new grid of models to be constructed, for future work.

5.6. The effect of NLTE

Figures 20 and 21 show the bolometric lightcurve and the spectral evolution of model 12C calculated with JEKYLL with and without non-thermal ionization and excitation. Before 10 days both the bolometric lightcurve and the spectral evolution are very similar, after which they start to differ in several aspects. This turning point coincides with the time when the radioactive energy deposition becomes important outside the photosphere (see Fig. 14). The most striking difference in the spectral evolution is the absence of (strong) helium lines in the model without non-thermal processes. This well-known effect was discussed in Sect. 5.2.2, and the result once more confirms those from earlier NLTE calculations by Lucy (1991) and Dessart et al. (2012).

Less known is the quite strong effect on the bolometric lightcurve, where the diffusion peak of the model with non-thermal processes is considerably broader. The reason for this is the increased degree of ionization, and therefore the increased electron scattering opacity. This is illustrated by Fig. 22, which shows the evolution of the electron fraction in the carbon-oxygen core and the helium and hydrogen envelopes. In the model with non-thermal processes, the electron fraction in the helium envelope drops much slower than in the model without. Due to the lower ionization potential, the effect is much less pronounced in the carbon-oxygen core and the hydrogen envelope. In **Fig. 20** we also show a model calculated assuming LTE for the excited levels of the ions (but not for the ionization balance), in a manner similar to what is done by ARTIS. This model shows an even narrower bolometric lightcurve, which is related to the even lower degree of ionization in this model.

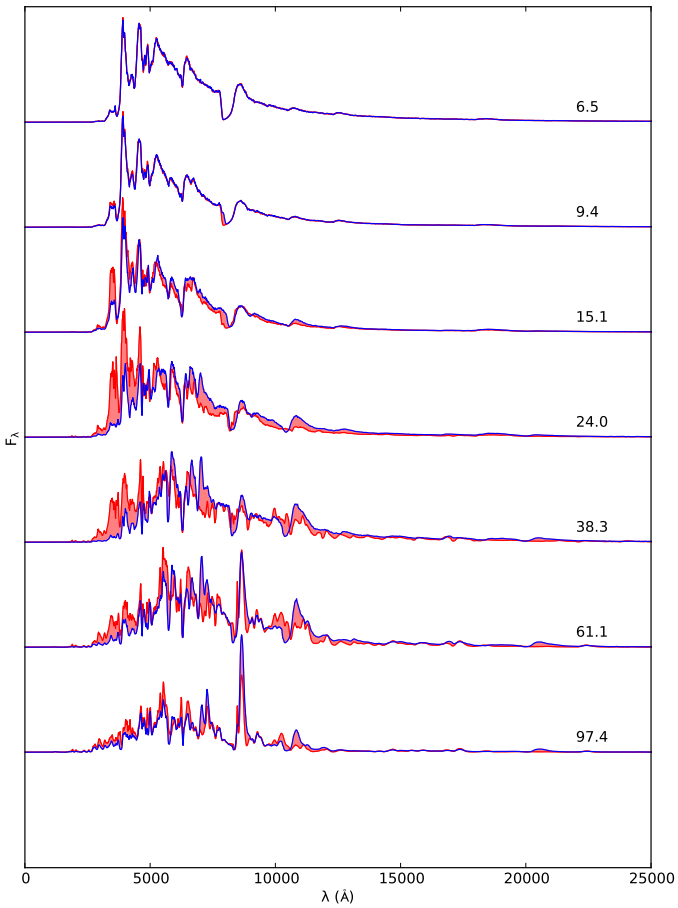

Fig. 21. Spectral evolution for model 12C calculated with (blue) and without (red) non-thermal ionization and excitation, **where the difference has been highlighted in shaded red**.

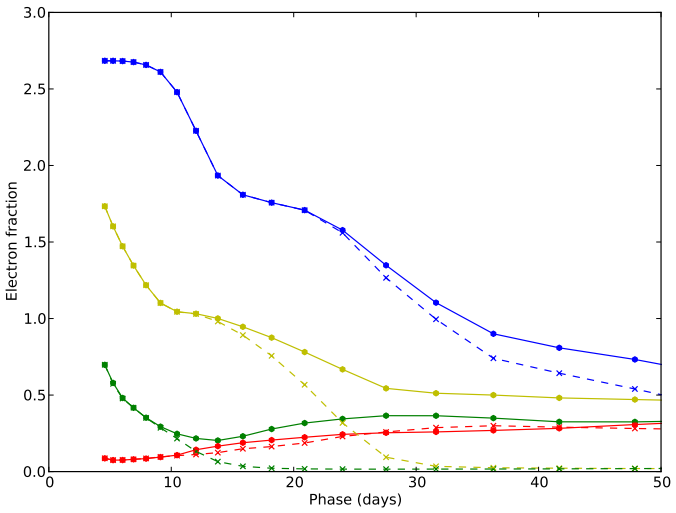

Fig. 22. Evolution of the electron fraction in the oxygen core (blue), inner/outer (yellow/green) helium envelope and the hydrogen envelope (red) for model 12C calculated with (circles and solid lines) and without (crosses and dashed lines) non-thermal ionization and excitation.

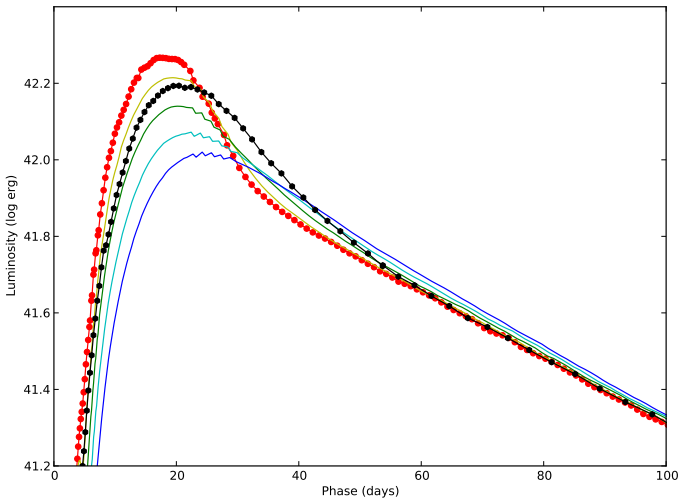

Fig. 23. Bolometric lightcurve for model 12C as calculated with JEKYLL (black circles) and the bolometric lightcurve for model 12C calculated with HYDE using an opacity floor of 0.024 (red circles), 0.05 (yellow line), 0.1 (green line) 0.15 (cyan line) and 0.2 (blue line) cm^2 g^{-1}.

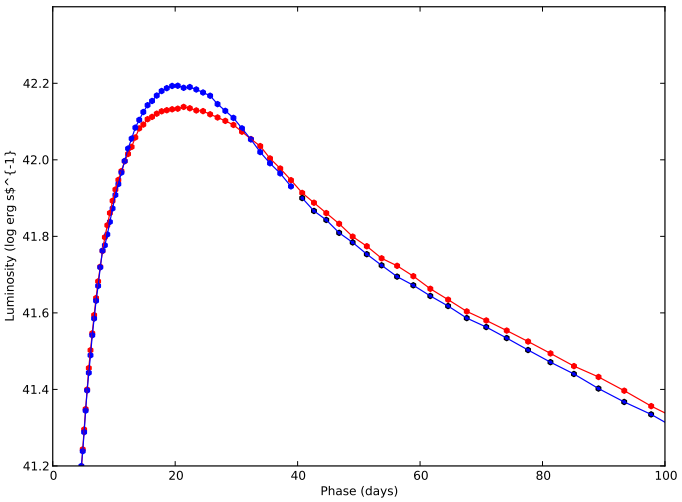

Fig. 24. Bolometric lightcurve for model 12C as calculated with JEKYLL using macroscopic (blue) and microscopic (red) mixing.

In E15 we calculated the bolometric lightcurve for model 12C with the LTE-based code HYDE, and in Fig. 23 we show this lightcurve together with the one calculated by JEKYLL. HYDE uses opacities calculated for a static medium in LTE, and an opacity floor intended to mimic the effects of expansion and non-thermal ionization. However, the floor was calibrated to the hydrodynamical code STELLA (Melina Bersten, private communication) which does not include non-thermal ionization, so this effect is not taken into account. Comparing the bolometric lightcurves calculated with JEKYLL and HYDE, we see that the latter is considerably narrower, in line with the comparisons discussed above. Furthermore, as also shown in Fig. 23, a good match between the JEKYLL and HYDE calculations is not possible even if the opacity floor is increased, and a more elaborate parametrization of the HYDE opacity is required. In the literature, codes similar to HYDE are commonly used to calculate bolometric lightcurves, and our results highlight the need for full NLTE calculations to properly determine the opacities.

5.7. The effect of macroscopic mixing

Figures 24 and 25 show the bolometric lightcurve and the spectral evolution of model 12C calculated with JEKYLL using microscopic and macroscopic mixing of the material. Before 15 days both the bolometric lightcurve and the spectral evolution is very similar in the two mixing scenarios, after which the spectral evolution becomes increasingly different. The bolometric lightcurves also differ around the peak, but once on the tail the difference becomes quite modest. The largest differences are seen in the spectral evolution after ~40 days. In particular, the Ca II 8498,8542,8662 Å and [Ca II] 7291,7323 Å lines become much stronger, whereas the [O I] 6300,6363 Å line becomes much weaker in the microscopic mixing scenario. As was previously pointed out by Fransson & Chevalier (1989), this effect is caused by microscopic mixing of calcium, which is a very effective coolant, into the oxygen-rich zones. The difference gets even worse after 150 days (not shown), and it seems clear that macroscopic mixing needs to be taken into account, at least in the nebular phase, for the model to be realistic.

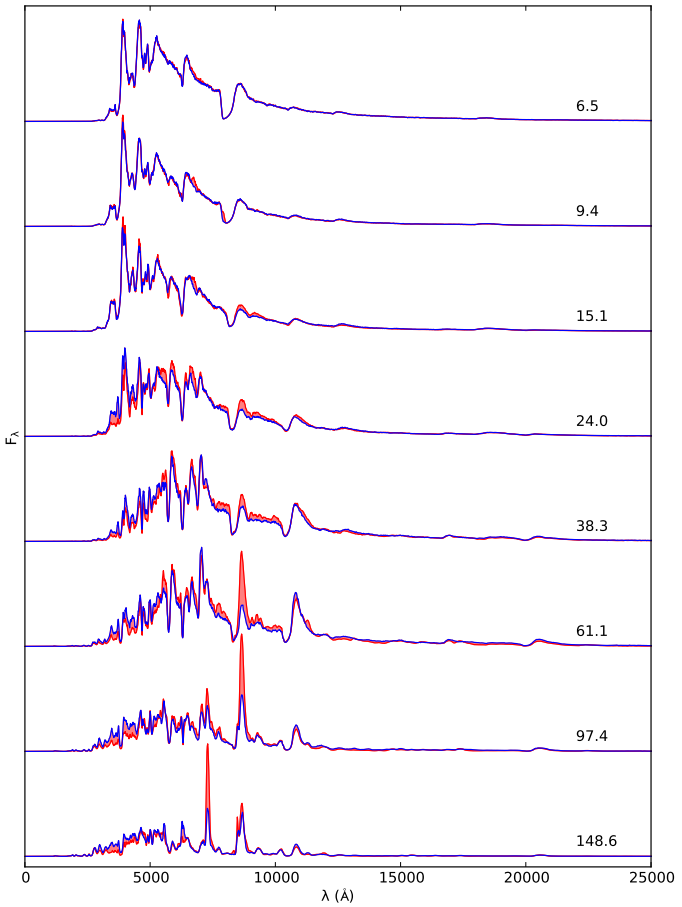

Fig. 25. Spectral evolution for model 12C as calculated with JEKYLL using macroscopic (blue) and microscopic (red) mixing. mixing, **where the difference has been highlighted in shaded red**.

6. Conclusions

We present and describe JEKYLL, a new code for modelling of SN spectra and lightcurves. The code assumes homologous expansion, spherical symmetry and steady state for the matter, but

is otherwise capable of solving for the time-evolution of the matter and the radiation field in full NLTE. In particular, it includes a detailed calculation of the non-thermal excitation and ionization rates **as well as a method to account for the macroscopic mixing that occurs in the explosion**. **We also present comparisons with ARTIS, SUMO and CMFGEN, three codes that are more or less similar to JEKYLL. The comparisons with ARTIS and SUMO are done using realistic models and provide tests of the time-dependent MC radiative transfer and the steady-state NLTE capabilities, respectively. The comparison with CMFGEN is done using a simplified test model, but provides a test of the full time-dependent NLTE capabilities of JEKYLL. All comparisons show a good agreement in the observed quantities as well as the state variables, and together they provide a good test of the JEKYLL code.**

We have applied JEKYLL to Type IIb SNe, by evolving the preferred J15 model for SN 2011dh through the early phase. This model, which has an initial mass of 12 $M_{\odot}$, was previously found to give a good agreement with the nebular spectra (J15) and lightcurves (E15), and here we find a reasonable agreement with the early spectra and lightcurves as well. Some quantitative differences exist, however, and to find a model that improves the agreement is a challenge to be addressed in future **work**. Nevertheless, most important observational aspects of SN 2011dh, many of which are observed in other Type IIb SNe as well, are well reproduced by the model. It also has much in common with the SE-SNe NLTE models by Dessart et al. (2015, 2016) evolved with CMFGEN, and in particular with the Type IIb model 3p65A. This demonstrates that our understanding of SN 2011dh and Type IIb SNe in general, has reached a rather mature level, and that NLTE modelling of such SNe is capable of producing realistic spectra and lightcurves.

We find strong effects of NLTE as well as macroscopic mixing on the spectra and the lightcurves, which shows that both of these effects are necessary for realistic simulations of SNe. In particular, NLTE effects are strong even on the bolometric lightcurve, which casts some doubts on LTE-based modelling of the bolometric lightcurve commonly used in the literature. For example non-thermal ionization turns out to have a strong effect on the ionization level in the helium envelope, which introduce a coupling between the mixing of the radioactive ^{56}Ni and the diffusion time not accounted for in LTE-based models. Further studies of the effects of NLTE and macroscopic mixing on the results are desirable, and promising topics for future papers.

Appendix A: Configuration and atomic data

Appendix A.1: Comparison to ARTIS

As much as possible, we have synchronized the configuration and the atomic data used by JEKYLL and ARTIS. To achieve this, both codes were configured to use a LTE solution for the matter based on T_J, **the temperature associated with the pure blackbody radiation field model (see Sect. 3.1.1 and K09), and the MC radiative transfer solver used by JEKYLL was configured to include radiative and collisional bound-bound and bound-free processes as well as free-free processes.** In addition, ARTIS was configured to use its grey approximation (see K09) before ∼6 days and below an optical depth of 100, and JEKYLL was configured to use the diffusion solver below an optical depth of 50.

The atomic data used by ARTIS is described in K09, but was restricted to the first four ionization stages, using the fourth as closure. As all of the atomic data is stored in data-files in a well-defined format, it was quite straight-forward to automatically convert it to the JEKYLL atomic data format, and it should be fully synchronized. ARTIS and JEKYLL were both configured to use a logarithmic time-step of 1 percent and single Λ-iteration per time-step, which is the standard procedure in ARTIS. As discussed in **Appendix B**, due to the short time-step, these runs are still well converged.

Appendix A.2: Comparison to SUMO

As much as possible, we have synchronized the configuration and the atomic data used by JEKYLL with that used for the modelling in J15. To achieve this, JEKYLL was configured to run in steady-state mode, and to use a full NLTE solution including the following; radiative bound-bound, bound-free and free-free processes, collisional bound-bound processes, non-thermal excitation, ionization and heating, as well as charge-transfer and two-photon processes. JEKYLL was also configured to use a recombination correction in a manner similar to SUMO (see J11), in which case detailed balance was not enforced.

The atomic data used for the modelling in J15 is described in J11 and Jerkstrand et al. (2012). In the case it was stored in data-files in a well-defined format, as for e.g. energy levels and spontaneous emission rates, it was automatically converted to the JEKYLL atomic data format, and otherwise it was added manually to the JEKYLL atomic data files based on the descriptions in J11 and Jerkstrand et al. (2012). Although not complete, the synchronization of the atomic data and the methods should be good enough for a meaningful comparison.

Appendix A.3: Comparison to CMFGEN

As much as possible, we have synchronized the configuration and the atomic data used by JEKYLL and CMFGEN. To achieve this, JEKYLL was configured run in time-dependent (radiative transfer) mode, and to use a full NLTE solution including the following; radiative bound-bound, bound-free and free-free processes, as well as collisional bound-bound and bound-free processes. In addition, JEKYLL was configured to use the time-dependent NLTE rate equations and to use the diffusion solver below an optical depth of 100.

The atomic data for the simpified composition of hydrogen, helium, oxygen and calcium were automatically converted from the well-defined format of CMFGEN to that of JEKYLL, and should therefore be fully synchronized. CMFGEN and JEKYLL were both configured to use a logarithmic time-step of 2.5 percent, and JEKYLL was configured to use 4 Λ-iterations per time-step. As discussed in Appendix. B, this gives a well converged solution.

Appendix A.4: Application to Type IIb SNe

JEKYLL was configured to run in time-dependent **(radiative transfer)** mode, and to use a full NLTE solution including the following; radiative bound-bound, bound-free and free-free processes, collisional bound-bound and bound-free processes, non-thermal excitation, ionization and heating, as well as two-photon processes. JEKYLL was also configured to use the diffusion solver below an optical depth of 50, and a recombination correction while still enforcing detailed balance. In addition, packet control (see Sect. 3.3.5) was turned on to assure good sampling of the radiation field in all frequency regions. The logarithmic time-step was set to 5 percent and the number of Λ-iterations per

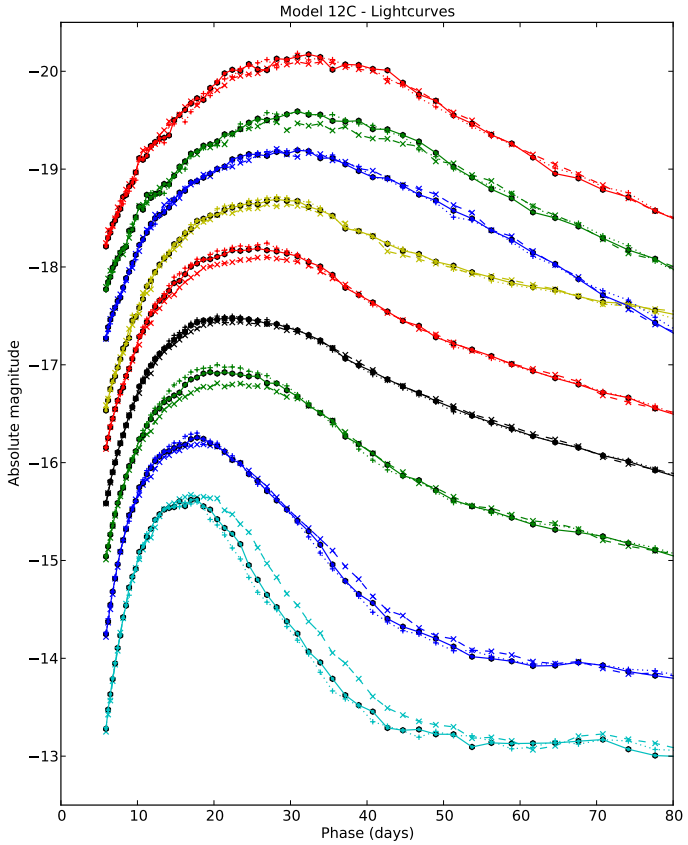

Fig. B.1. Broad-band and bolometric lightcurve for model 12C as calculated with JEKYLL using 2 (dashed lines and crosses), 4 (solid lines and circles) and 8 (dotted lines and pluses) Λ-iterations per time-step. Otherwise as described in Fig. 18.

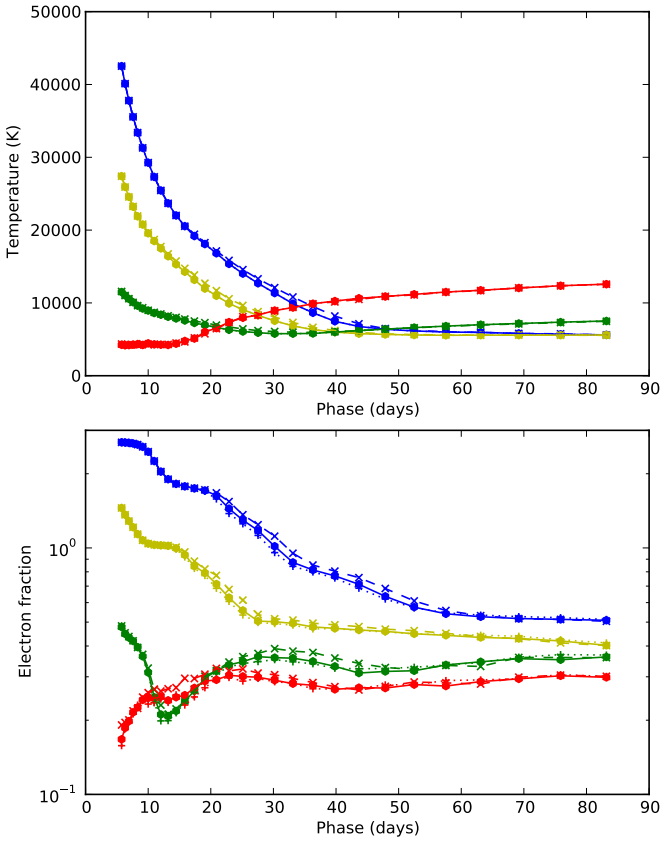

Fig. B.2. Temperature (upper panel) and electron fraction (lower panel) for model 12C as calculated with JEKYLL using 2 (dashed lines and crosses), 4 (solid lines and circles) and 8 (dotted lines and pluses) Λ-iterations per time-step. Otherwise as described in Fig. 8.

time-step was set to 4. As discussed in Appendix. B, this gives a well converged solution.

The atomic data used is the same as for the comparison with SUMO (Sect. A.2), but with the following modifications. The highest ionization stage was increased to VI for all species, and the stage III ions were updated to include at least 50 levels for elements lighter than Sc, and at least 200 levels for heavier elements, using online data provided by NIST[6] and R. Kurucz[7]. Total recombination rates for the stage III ions were adopted from the online table provided by S. Nahar[8] whenever available, and otherwise from Shull & van Steenberg (1982). For ionization stages IV to VI we only included the ground-state multiplets, adopted the photo-ionization cross-section by Verner & Yakovlev (1995) and Verner et al. (1996) and assumed the populations to be in LTE with respect to stage IV.

Appendix B: Convergence of the Λ-iterations

As discussed in Sect. 3, JEKYLL use a fixed (but configurable) number of Λ-iterations. In time-dependent **(radiative transfer)** mode, this is the number of Λ-iterations per time-step, and corresponds to some (unknown) number of effective Λ-iterations depending on the length of the time-step and the rate at which the state is changing. The time-dependent NLTE runs in Sect. 5 use a logarithmic time-step of 5 percent and 4 Λ-iterations per time-step. In Figs. B.1 and B.2 we show the lightcurves and the temperature and electron fraction, respectively, for three such runs using 2, 4 and 8 Λ-iterations per time-step. As can be seen, convergence is fast, and more than 4 iterations per time-step does not make a significant difference. Even the 2-iterations run is good enough for most purposes, although there is a ∼25 percent difference in the U-band during the drop from the peak onto the tail. The time-dependent LTE runs in Sect. 4.1 **behave** in a similar way, but the shorter time-step of 1 percent, and possibly a faster convergence in the LTE case, **make** even a single iteration run well converged, showing less discrepancy than the 2-iterations run in Figure B.1. **In the case of the time-dependent NLTE runs in Sect. 4.3, using more than 4 Λ-iterations per time-step does not make a significant difference, and using 4 instead of 2 Λ-iterations only marginally changes the spectra.**

[6] www.nist.gov
[7] http://www.cfa.harvard.edu/amp/ampdata/kurucz23/sekur.html
[8] http://www.astronomy.ohio-state.edu/~nahar/_naharradiativeatomicdata/

References

Abbott, D. C. & Lucy, L. B. 1985, ApJ, 288, 679
Bersten, M. C., Benvenuto, O. G., Nomoto, K., et al. 2012, ApJ, 757, 31
Dessart, L. & Hillier, D. J. 2008, MNRAS, 383, 57
Dessart, L. & Hillier, D. J. 2010, MNRAS, 405, 2141
Dessart, L., Hillier, D. J., Li, C., & Woosley, S. 2012, MNRAS, 424, 2139
Dessart, L., Hillier, D. J., Woosley, S., et al. 2015, MNRAS, 453, 2189
Dessart, L., Hillier, D. J., Woosley, S., et al. 2016, MNRAS, 458, 1618
Ergon, M., Jerkstrand, A., Sollerman, J., et al. 2015, A&A, 580, A142
Ergon, M., Sollerman, J., Fraser, M., et al. 2014, A&A, 562, A17
Falk, S. W. & Arnett, W. D. 1977, ApJS, 33, 515

Fransson, C. & Chevalier, R. A. 1989, ApJ, 343, 323
Hillier, D. J. & Dessart, L. 2012, MNRAS, 424, 252
Hillier, D. J. & Miller, D. L. 1998, ApJ, 496, 407
Hubeny, I. & Mihalas, D. 2014, Theory of Stellar Atmospheres
Jerkstrand, A., Ergon, M., Smartt, S. J., et al. 2015, A&A, 573, A12
Jerkstrand, A., Fransson, C., & Kozma, C. 2011, A&A, 530, A45
Jerkstrand, A., Fransson, C., Maguire, K., et al. 2012, A&A, 546, A28
Kasen, D., Thomas, R. C., & Nugent, P. 2006, ApJ, 651, 366
Kerzendorf, W. E. & Sim, S. A. 2014, MNRAS, 440, 387
Kozma, C. & Fransson, C. 1992, ApJ, 390, 602
Kozma, C. & Fransson, C. 1998, ApJ, 496, 946
Kromer, M. & Sim, S. A. 2009, MNRAS, 398, 1809
Liu, Y.-Q., Modjaz, M., Bianco, F. B., & Graur, O. 2016, ApJ, 827, 90
Lucy, L. B. 1991, ApJ, 383, 308
Lucy, L. B. 2002, A&A, 384, 725
Lucy, L. B. 2003, A&A, 403, 261
Lucy, L. B. 2005, A&A, 429, 19
Marion, G. H., Vinko, J., Kirshner, R. P., et al. 2013, ArXiv e-prints
Maund, J. R., Fraser, M., Ergon, M., et al. 2011, ApJ, 739, L37
Mazzali, P. A. & Lucy, L. B. 1993, A&A, 279, 447
Olson, G. L., Auer, L. H., & Buchler, J. R. 1986, J. Quant. Spec. Radiat. Transf., 35, 431
Paxton, B., Bildsten, L., Dotter, A., et al. 2011, ApJS, 192, 3
Paxton, B., Cantiello, M., Arras, P., et al. 2013, ApJS, 208, 4
Scharmer, G. B. 1984, Accurate solutions to non-LTE problems using approximate lambda operators, ed. W. Kalkofen, 173–210
Shull, J. M. & van Steenberg, M. 1982, ApJS, 48, 95
Sobolev, V. V. 1957, Soviet Ast., 1, 678
Stritzinger, M. D., Taddia, F., Burns, C. R., et al. 2017, ArXiv e-prints
Taddia, F., Sollerman, J., Leloudas, G., et al. 2015, A&A, 574, A60
Taddia, F., Stritzinger, M. D., Bersten, M., et al. 2017, ArXiv e-prints
Verner, D. A., Ferland, G. J., Korista, K. T., & Yakovlev, D. G. 1996, ApJ, 465, 487
Verner, D. A. & Yakovlev, D. G. 1995, A&AS, 109, 125
Werner, K. & Husfeld, D. 1985, A&A, 148, 417
Woosley, S. E., Eastman, R. G., Weaver, T. A., & Pinto, P. A. 1994, ApJ, 429, 300
Woosley, S. E. & Heger, A. 2007, Phys. Rep., 442, 269